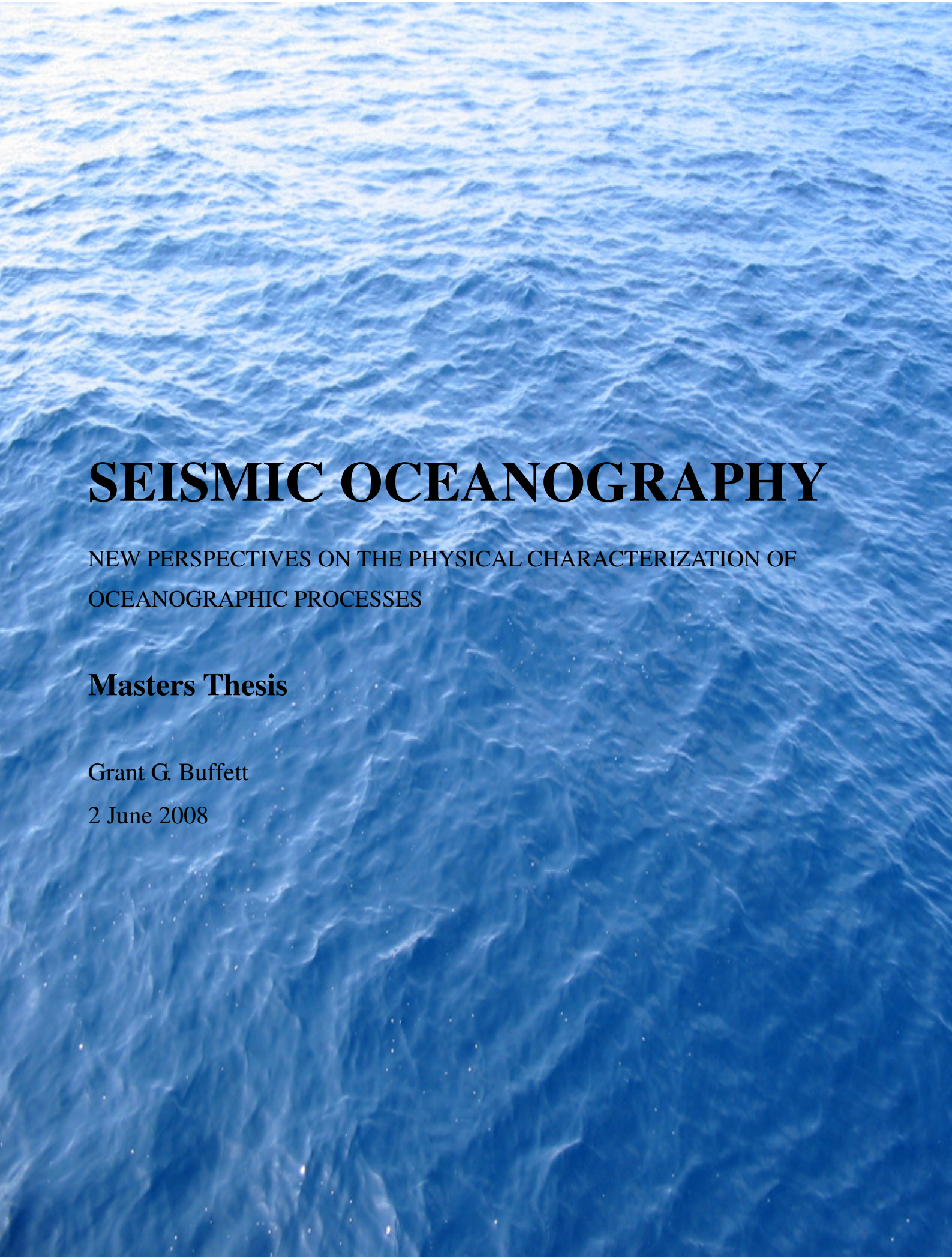

SEISMIC OCEANOGRAPHY

NEW PERSPECTIVES ON THE PHYSICAL CHARACTERIZATION OF OCEANOGRAPHIC PROCESSES

Masters Thesis

Grant G. Buffett

2 June 2008

PREFACE

In this research I present details on the new seismic oceanography method. I apply seismic reflection profiling to study large scale thermohaline structures and ocean current circulation in the Gulf of Cadiz and western Iberian coast. Since circulation within the ocean is important for the redistribution of heat on our planet and its influence on climate, I analyze seismic data from the study region to gain knowledge of the Mediterranean Undercurrent and corroborate this with historical oceanographic data.

In the ocean, water masses of different temperature and salinity are stratified and separated by thin boundary layers. Conventional oceanographic techniques have been able to image these boundaries, however only at sparse horizontal intervals. To image these boundaries, I use the multi-channel seismic reflection method, because it is a robust, well-tested method and has recently been shown to be suitable for imaging the ocean's boundary layers with a horizontal resolution, some two orders of magnitude greater than conventional oceanographic techniques. In this way, seismic reflection profiling is emerging as a new tool to study the ocean on a large scale thus helping oceanographers visualize these boundary layers with unprecedented resolution.

Seismic waves travel through liquids as pressure waves which refract and reflect according to density and sound speed variations. When a wave front impinges upon an acoustic impedance boundary there is partial transmission and partial reflection depending on the ratios of density and sound speed above and below the boundary. At any given pressure, temperature and salinity are the dominant factors influencing density and sound speed in the ocean. However, the precise contribution from each is not well known and may vary considerably in different regions or in different mixing regimes.

In the Gulf of Cadiz, Mediterranean Water that is characterized by a relatively high temperature and salinity signature due to excess evaporation in the Mediterranean Sea, overflows the Strait of Gibraltar at depth and equilibrates with the surrounding Atlantic water masses. The Mediterranean Water entrains water from the overlying North Atlantic Central Water mass and therefore mixes and becomes diluted. These starkly contrasting water masses is precisely what makes this region an ideal test bed for seismic reflection profiling and allows us to address some of the characteristics and ocean dynamic processes in the region.

The Mediterranean Undercurrent, is an intermediate depth-jet current that flows from the source of Mediterranean Water at the Strait of Gibraltar, westward, guided by buoyancy and bathymetry then is directed northward along the coast of Iberia due to the Coriolis effect. It is suspended at depth, surrounded by the North Atlantic Central Water above and the North Atlantic Deep

Water below. Its contrasting high salinity and temperature profile induces internal stratification and stimulates mixing processes. Processing and analysis of archived seismic data recorded over the flow path of the Mediterranean Undercurrent are able to image internal structures such as lateral stratification, evidence of turbulence and Meddies, large, meso-scale Mediterranean Water eddies. The objective of this work is to corroborate seismic and historical oceanographic data in the region thereby using seismic reflection profiling to characterize physical oceanographic processes.

1 – INTRODUCTION

Ocean dynamics have long been the subject of much interest. Its significance has long been recognized. However in recent decades we have been able to study the ocean and its dynamics with unprecedented detail and accuracy, telling us more about the physical, biological and chemical processes that control it and therefore, how we affect and are effected by it. Modern physical oceanography involves measurements of temperature, salinity and density variations in the ocean as well as the study of waves, tides and currents, the ocean-atmosphere interaction and the properties of seawater such as the propagation of light and sound, [Knauss, 1997].

Our ability to construct models that represent physical oceanographic phenomena and our increasing knowledge of these phenomena elucidate the ocean's role in the distribution of heat around the planet and the effect this has on climate. Density variations in the ocean affect its dynamics since differences in weight cause pressure differences, which drive motion, if unopposed. These density driven currents are controlled by buoyancy forces and are generally a result of temperature and/or salinity variations caused by heat fluxes at the boundaries of fluids, [Thorpe, 2005].

The more information we can gather about density variations in the ocean, the more we can learn about ocean dynamics and heat redistribution. Seismic reflection profiling addresses these density variations by measuring the degree of acoustic energy reflected from impedance boundaries, the amount of reflected energy being proportional to the density and sound speed contrasts across the interface. Stronger contrasts mean increased reflection and decreased transmission of the impinging wave front. This reflected energy is recorded by seismometers and processed to create a large scale 'reflectivity map' of the ocean. The high degree of correlation between in situ sound speed measurements and seismic reflectivity is remarkable, demonstrating the potential of seismic reflection profiling as a new tool through which to study the ocean.

There have been numerous treatises published on using acoustic methods to measure ocean fluid dynamic properties since significant initial research by Obukhov, [1941], [eg. Batchelor, 1957; Chernov, 1957; Ottersten, 1969; Tatarski 1971; Munk and Garrett, 1973; Brandt, 1975; Goodman 1990]. Brandt, [1975] studied high-frequency sound scattering from density variations of a turbulent saline jet in the laboratory. He concluded that the observed scattering was a result of acoustic impedance fluctuations produced by the jet and therefore surmised that acoustic imaging techniques could be used to study oceanic diffusion processes and thermohaline structures. Orr and Hess, [1978] acquired a joint physical oceanography/multi-frequency high-frequency acoustic backscatter dataset and observed that at depths corresponding to the temperature gradient maximum there was increased backscatter intensity. To this end, they asserted that oceanic microstructure played a role.

Following this work, Haury et al., [1983] provided further constraints on the relationship between oceanic microstructure and acoustic backscatter. By combining the methods of Orr and Hess with plankton measurement constraints, they were able to produce an acoustic snapshot of an ostensibly breaking internal wave, thereby identifying thermohaline fine structure as the source of the backscatter. Munk and Wunsch, [1979] first used travel-time ocean acoustic tomography by adapting a technique used in seismology to image the interior of the earth to represent large scale ocean structures.

Thorpe, [2005] describes backscatter reflection from turbulent microstructure in the frequency range of 100-200 kHz saying that the acoustic return from a 'clear water' scattering region, meaning one devoid of algae, bubbles or particles, depends on range and attenuation in the water column as well as the acoustic cross-section of the scattering volume and the sound frequency.

Notwithstanding the aforementioned acoustic techniques, the ocean has not been extensively explored with seismic waves, although many reflection seismology surveys have been conducted over the oceans to explore the solid Earth. Since this work deals with imaging thermohaline finestructure in the ocean by measuring acoustic impedance contrasts, in the next section I present an overview of the fundamentals of the seismic reflection method as it pertains to physical oceanography.

2 - THE SEISMIC REFLECTION METHOD

Seismic reflection profiling generally proceeds in four stages: survey design, acquisition, processing and interpretation. The design stage involves choosing the site to perform the experiment and the acquisition parameters necessary. It is important at this point to clearly know the objective of the study such as to provide constraints and minimize unknowns. A well planned survey can avoid problems at later stages. Ideally, acquisition of seismic data progresses according to plan, however there may be unforeseen circumstances, which require logistical or implementation changes in the survey. Ease of processing follows from a well designed and well implemented profile. Cooperation between field crews and processing scientists is important. Finally, the interpretation of seismic data depends upon knowledge of all previous stages. An accurate, informative interpretation can only result from a well planned, well executed and correctly processed data set. The following three subsections discuss in detail, acquisition, processing and interpretation of seismic reflection data.

2.1 – ACQUISITION

Seismic reflection profiling has been successfully used for decades to image the subsurface of the earth. It is a well tested method first described by Reginald Fessenden and developed by the hydrocarbon industry to aid in the exploration of oil and gas, [Finch, 1985]. Initial surveys in the first part of the 20th century involved one shot and one receiver on the surface with a known separation (offset). The time from the first shot to the first detection of upgoing energy in the receiver was used to calculate the depth to the reflecting interface. However, many assumptions were needed to make this calculation. The subsurface was considered to be homogeneous and isotropic and the reflecting interface, horizontal. Furthermore, the depth to the interface, relative to the source-to-receiver separation was assumed to be very large, thus approximating the source and receiver to be effectively co-located, thereby measuring a near zero-offset reflection. Although replete with assumptions, the method allowed the first proof-of-concept for seismic reflection.

Modern marine seismic reflection surveys are done by a large ship towing an impulsive source and a streamer (a cable filled with hydrophones) which record both signal and noise (figure 1). The acoustic energy travels through the water column and the Earth's crust, while becoming attenuated and losing energy through spherical divergence. Acoustic impedance boundaries defined by varying density and sound speed modify the transmission to reflection ratio. Transmitted energy is absorbed by the ocean and solid earth and converted to other forms of energy (eg. kinetic energy, heat). Reflected energy, also being attenuated somewhat, is recorded by the towed streamer and stored for later processing.

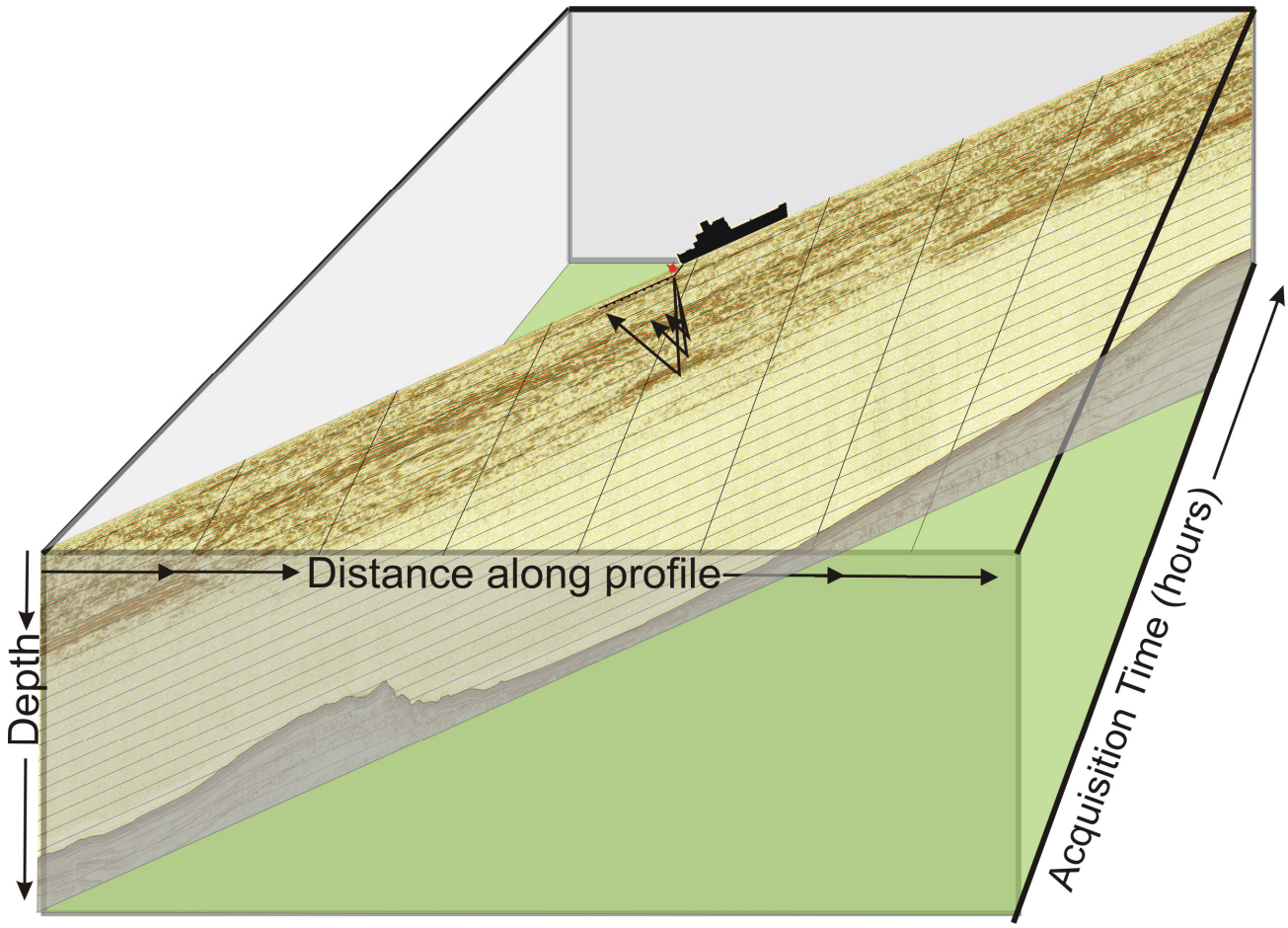

Figure 1 – Illustration of seismic acquisition and the "near real-time" imaging effect of seismic oceanography. Due to the nature of large scale ocean circulation, currents may change appreciably on the order of the acquisition time, making seismic oceanography inherently 2D+time.

2.1.1 - SEISMIC SOURCES AND RECEIVERS

In marine seismic surveys, dynamite has been long replaced by air guns as the source, which release a known volume of compressed air into the water column. Impulsive sources have a distinct wavelet shape, which is characterized by the majority of the energy being front-loaded, that is, confined to the beginning of the wavelet, with a quickly decaying coda. This is referred to as minimum phase, [Yilmaz 1987].

The first seismic receivers were electromagnetic devices that operated by a magnet forced to oscillate vertically through a coil of wire by the reflected seismic wave, thus inducing a current which is then plotted as an analog time series. More recent receivers use piezoelectric materials to perform the same task. Finely sampled digitization of the data then approximates the analog signal to a high degree, thus allowing user processing and analyses through decomposition of the signal into its frequency, amplitude and phase components.

2.1.2 - THE COMMON MIDPOINT METHOD

One of the most significant advances in seismic reflection profiling came with the common-midpoint (CMP) method. This method of acquisition design took advantage of the redundancy of sources and receivers to produce a continuous image of the subsurface as well as to minimize noise. In this method, instead of a single source and receiver, there is an array of sources and receivers at regular intervals with varying source-receiver offsets. The CMP method makes an assumption that time differences between individual traces within a CMP gather are not affected by structural differences, [Cox, 1999]. This assumption is not strictly true in many cases, such as crooked-line surveys, and in marine surveys where the towed receiver streamer experiences 'feathering' due to near-surface currents. In such cases 'binning' of midpoints is necessary to group common midpoints into user defined groups (or, bins), [Cox, 1999].

2.2 – PROCESSING

Processing of seismic data starts with discrete sampling of the continuous analog signal into a digital waveform. This allows the advantage of decomposing the wavelet into its individual samples and organizing (sorting) it such as to allow detailed analysis of the data. The more frequently the continuous signal is sampled, the more the resulting digital signal approaches the true analog signal. For the extreme case of a zero sampling interval, the analog signal can be fully represented, [Yilmaz 1987]. In practice however, the sample rate is chosen by weighing the necessary resolution needed to image the target against available computing hardware limitations such as disc space and CPU speed.

2.2.1 – DIGITIZATION

There are a number of things to consider when digitizing seismic data. Primarily, one must avoid under sampling the data, such as not to lose higher frequency field data above the Nyquist frequency. The Nyquist frequency is the maximum recoverable frequency bandwidth when digitizing data. It is given by the expression,

$$f_n = \frac{1}{2(\Delta t)}$$

eq. 1

where f_n is the Nyquist frequency and Δt is the sample rate. Therefore, if the analog signal is sampled at an interval of 4 ms, the maximum recoverable frequency is 125 Hz, whereas at 2 ms, frequencies up to 250 Hz can be recovered. The maximum temporal (vertical) resolution available in the seismic data

is accordingly a function of frequency and is commonly expressed as 1/4 of the wavelength, [Widess, 1973]. The coarser the sampling interval, the smoother the digitized signal, which results in the loss of the higher frequency components of the data, [Yilmaz, 1987]. Therefore, when sampling an analog signal, it is necessary to consider the resolution one needs to image the reflection target in question. Physical oceanographic targets that pertain to meso-scale or large scale mixing processes are typically on the order of 10's of meters to kilometer scales, [Knauss, 1997].

2.2.2 - THE FOURIER TRANSFORM

The Fourier Transform is fundamental to seismic data analysis and applies to nearly all stages of processing. It converts a time function into its frequency domain representation and vice-versa, [Sheriff, 1991]. Any given time series can be decomposed into its individual frequency components through the forward Fourier transform. Likewise, given the individual frequency components, a synthetic seismic trace can be constructed fully and completely through the inverse Fourier transform, [Yilmaz, 1987]. The Fourier transform is defined by the relation,

$$\mathcal{X}(\omega) = \int_{-\infty}^{\infty} x(t) \exp(-i\omega t)\, dt$$

eq. 2

where ω is angular frequency, given by $\omega = 2\pi f$, where f is frequency and t is time. Similarly, the inverse Fourier transform is given as,

$$x(t) = \int_{-\infty}^{\infty} \mathcal{X}(\omega) \exp(i\omega t)\, d\omega$$

eq. 3

When an analog signal is sampled into a discrete time series, the digital signal is reconstructed based on the number of samples. However, the reconstructed signal will inevitably lack the details from the analog signal, which are manifested in the higher frequency components, [Yilmaz, 1987]. These higher frequency samples are not lost by digitization. They are folded-back or 'wrapped around' and appear as lower frequency components below the Nyquist. This is the undesirable result of digitization caused by undersampling.

2.2.3 - DATA SORTING

Digitized data are able to be sorted and thus manipulated in many ways. Each seismic trace, (and its data samples) has an associated data header value which contains information on the basis of which we can sort. When samples and traces are acquired in the field, they are acquired time sequentially. That is, for trace 1, sample 1, trace 2, sample 1, trace 3, sample 1, etc... But it is helpful for the purpose of visualizing acoustic impedance boundaries to have data sorted trace sequentially. That is, trace 1, samples 1,2,3…, trace 2, samples 1,2,3…, etc... This conversion is done through a matrix routine, called demultiplexing and is one of the first steps in data processing, [Sheriff, 1991]. Once traces are demultiplexed, they are ready to be further sorted in useful ways. It is common to begin with traces sorted as common shot gathers (figure 2).

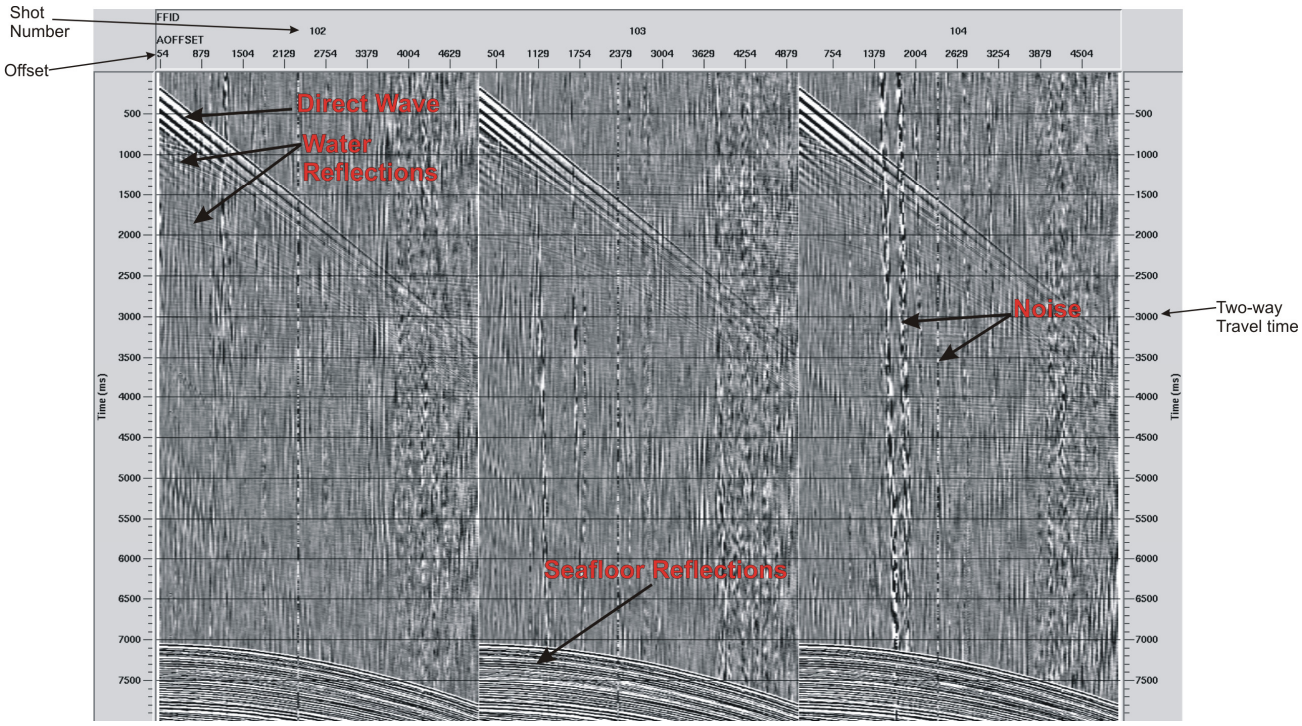

Figure 2 – Three labeled shot records showing location of prominent events. Note the large amplitude seafloor reflections and direct wave compared to the water reflections.

Traces sorted by shot are now more geometrically representative of the subsurface. The linear direct wave is shown emanating from the source at the surface and becoming deepest at the farthest offset. The acoustic impedance reflections are shown as hyperbolae and have a lower amplitude than the direct wave. Since this is a shot from a marine survey, we can see water column reflections, seafloor reflections and those beneath the seafloor.

To approximate a zero-offset seismic section we first sort the traces by their common midpoints. Ideally, we would like to record acoustic reflections from directly below the source, so we can

minimize unknowns such as anisotropic velocity variations in the ray path. But, in practice this is impossible due to the noise generated from the source distorting the signal arriving at the receiver. The common midpoint method therefore, allows us to image a point in the subsurface as if the source was directly above, halfway between source and receiver.

2.2.4 – DECONVOLUTION

Deconvolution is a wavelet shaping process designed to restore the original seismic wavelet as it was before the effect of linear filtering by the medium, [Sheriff, 1991]. The primary objective of seismic data processing is to recover the reflection series from recorded traces such that they can represent the layering (acoustic impedance contrasts) in the earth, or in the case of seismic oceanography, in the water column. In addition to improving temporal resolution, deconvolution can suppress multiples (reflected energy that has reflected multiple times, thus delaying its arrival and appearing as a deeper reflection event). However, since deconvolution whitens the spectra as it increases resolution, it may also enhance high frequency noise.

2.2.5 - STATICS CORRECTIONS

Static time shifts in seismic data (statics) are present for various reasons and should be corrected to improve the stacked section. Principally, statics corrections are needed to correct for low, near surface velocity variations or significant elevation changes which delay the arrival of the reflected seismic signal such that adjacent traces of the same reflector may be misaligned, [Cox, 1999]. Given the flatness of the ocean surface compared to topographic relief and the very small variation in sound speed within in the water column, static shifts are not significant in seismic oceanography.

2.2.6 - VELOCITY ANALYSIS AND NORMAL MOVEOUT CORRECTION (NMO)

For a given CMP gather, in order to correct for the effect of normal moveout, that is, the effect of increasing reflection travel time with longer offset receivers (traces), one needs to apply an appropriate shift in stacking velocity to flatten the hyperbolic reflectors as if the receivers were all located at zero-offset. Stacking velocity is the chosen velocity function used for NMO correction that yields the best stacking response, [Hatton et al., 1986]. In this way stacking velocity is somewhat cosmetic. However, it approximates the NMO velocity. That is, while the NMO velocity is based on the small spread hyperbolic travel-time, [Taner and Koehler, 1969], stacking velocity is based on the hyperbola that best fits the data over the entire spread length, [Yilmaz, 1987]. The numerical representation of normal moveout correction is given as,

$$\Delta t_{NMO} = t(0)\left\{\left[1+\left(\frac{x}{v_{NMO}t(0)}\right)^2\right]^{½} - 1\right\}$$

eq. 4

where t(0) is the two-way travel time along a vertical path, x is offset, and v_{NMO} is the sound speed of the medium before the reflecting interface. Seismic velocity can vary both horizontally and vertically, so it is necessary to pick a vertically varying velocity function at various locations along the profile to correct for normal moveout (figure 3).

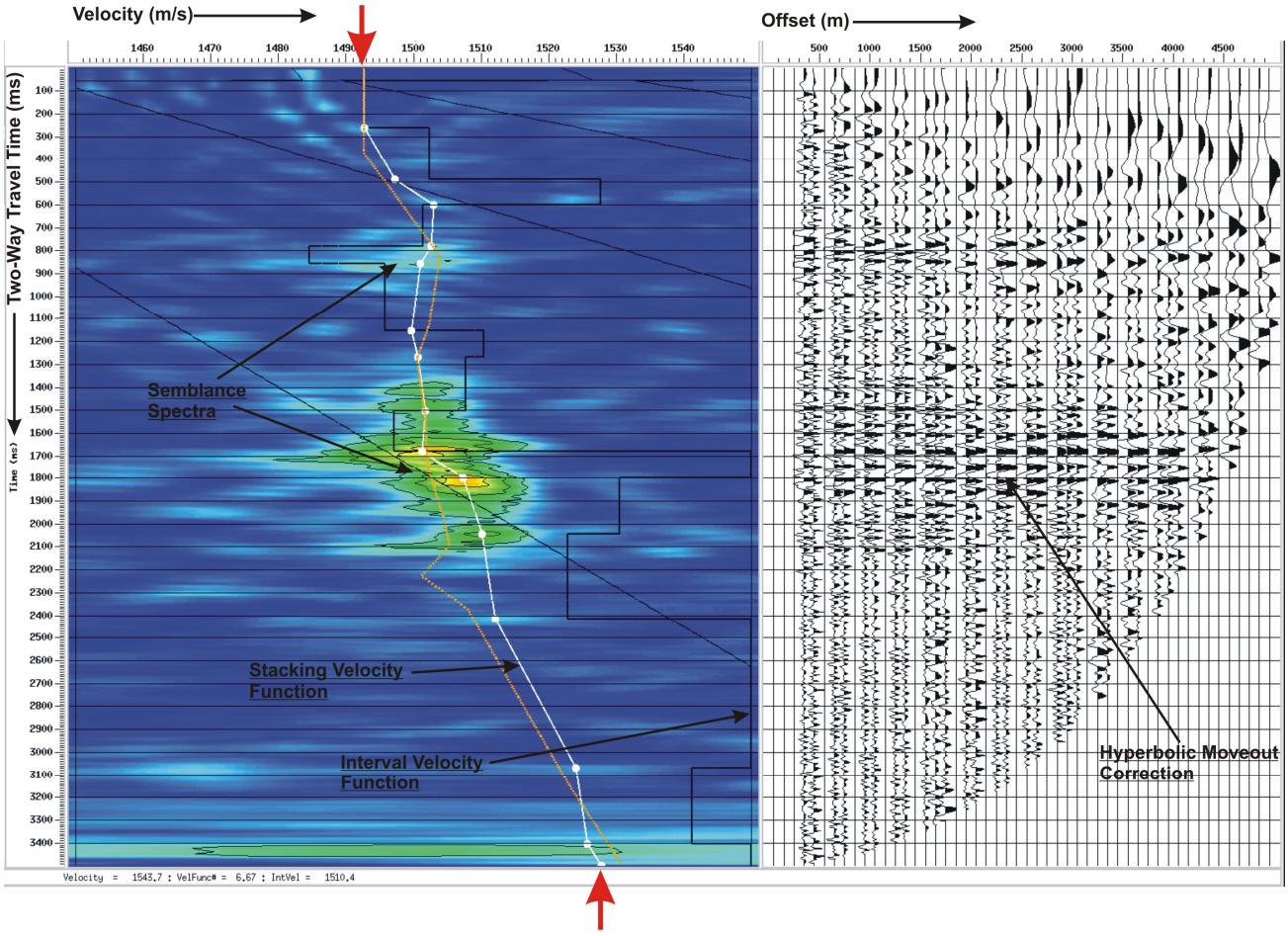

Figure 3 – Velocity Analysis of water column reflections in the Gulf of Cadiz showing prominent features. Note the narrow range in stacking velocity variation (1493 m/s to 1528 m/s for this velocity panel), indicated by red arrows.

In seismic oceanography, different from in the solid earth, seismic velocities vary minimally, and indeed an assumed constant water sound speed of approximately 1500 m/s will produce a stack (zero-offset section), yet velocity analysis is necessary and does improve the final stack, especially in the shallow ocean, where, like in stratified rock layers, shallower interfaces are more sensitive to

stacking velocity adjustments. Nonetheless, we observe a general trend of increasing stacking velocity with depth in the ocean. Thorpe, 2005 points out that the speed of sound in water varies with temperature and, near the surface it is observed to increase by $3.6ms^{-1}$ per 1 K increase in temperature at 10°C and 35 psu (psu is the 'practical salinity unit' and refers to the amount of dissolved salts in parts per thousand). Moreover, confining pressure increases linearly with depth (in the absence of salinity or temperature variations), causing seawater compression. This results in adiabatic heating, thus compensating somewhat for decreasing temperature with depth as a consequence of the distance from maximum solar input at the surface, [Thorpe, 2005].

NMO stretching is the undesirable side-effect of, while correcting for normal moveout, that samples are differentially shifted, producing a non-linear distortion in wavelet shape, [Hatton et al., 1986]. NMO frequency distortion is quantified by,

$$\Delta f/f = \Delta t_{NMO}/t(0)$$

eq. 5

where f is the dominant frequency, Δf is the change in frequency and Δt_{NMO} is given by equation 4.

2.2.7 – STACKING

Common midpoint stacking is the process of summing together traces that share a common midpoint between source and receiver. It is thus the redundancy of many common midpoints that will increase the signal to noise ratio, because adjacent traces will combine constructively (signal) and deconstructively (noise), [Sheriff and Geldart, 1982]. Stacking compresses the offset dimension thereby reducing the data volume to the plane of a zero-offset section, [Yilmaz, 1987]. Any given sample recorded at any given time contains a degree of random noise. After correcting for normal moveout, adjacent traces in a CMP gather that record the same reflection event will contain different variations of random noise such that summing these traces has the effect of emphasizing signal and suppressing random noise. To this end, stacking is a powerful tool to statistically improve the signal-to-noise ratio of seismic data. Quantitatively, the mean sample value for a given two-way travel-time is calculated and we define the sample values on trace i as $a_i(t)$, the mean given by the relation,

$$A(t)=\frac{1}{N}\sum_{i=1}^{N} a_i(t)$$

eq. 6

2.2.8 – MIGRATION

Sheriff, [1991] describes seismic migration as an inversion operation involving rearrangement of seismic information elements such that events are displayed at their true subsurface locations. Migration moves dipping reflections up-dip and collapses diffraction hyperbolae. It adjusts dipping interfaces because energy reflected from dipping horizons does not arrive at the same time as energy from a horizontal interface for any given offset. In the physical interpretation of seismic data therefore, migrated data correctly positions reflections, [Hatton et. al., 1986]. Ideally, migration requires a priori knowledge of the velocity structure of the media in question, but in practice this is not known and must be arrived at iteratively through velocity analysis. However, co-located and simultaneously recorded in-situ oceanographic sound speed measurements (that is, an acoustic velocity model) have the potential to more accurately represent the migration velocity field than velocity analysis iterations alone. Although sound speed propagation in the ocean varies minimally, it does vary. Therefore, these fine variations are better sampled with oceanographic instruments and then used as the basis for seismic velocity analysis.

In a layer-cake structure, without lateral velocity variation, time-migration will suffice. But, when there is significant lateral velocity variation, a true representation of the subsurface should include a depth migration. Currently, keeping in mind the very small variation in acoustic water velocity, only time migration was tested. However, a comparative analysis of time and depth migrations may be informative.

2.2.9 - SECONDARY PROCESSES (DATA PRE-CONDITIONING)

Frequency filtering

Filtering is done in the frequency domain to limit the frequency content of the data. This may have the effect of improving the signal-to-noise ratio. Normally band-pass filtering is designed to be zero-phase, meaning it does not modify the phase spectrum of the of the input traces, but only band limits its amplitude spectrum, [Yilmaz, 1987]. Given an input seismic trace (time series) you apply a Fourier transform to resolve it into its individual frequency components. In the frequency domain the amplitude spectrum can then be shaped to the desired frequency characteristics. In general, seismic data usually contains some low and high frequency noise (eg. ocean swell and electrical noise, respectively). In practice, a ramping taper at each end of the pass band taking the shape of a trapezoid is necessary to avoid ringing caused by a sudden drop in frequency that is the result of a "boxcar shape" in the amplitude spectrum, [Yilmaz, 1987]. Typically, seismic energy is confined to a range of some 10-100 Hz, however recent experiments in seismic oceanography have tested frequencies up to 200 Hz with good results (see section 5 for details). Band-pass filtering can be applied pre or post

stack to optimize signal over noise and improve the stacked image.

Spherical divergence correction

Due to both geometrical spreading and physical attenuation in the medium, acoustic energy measured at the surface is attenuated. Therefore, samples which correspond to any given acoustic impedance boundary are amplitude reduced by a factor dependent upon the ray path as well as the attenuation properties of the media themselves. Geometrical spreading in flat media (that is, for shallow depths relative to the diameter of the planet) accords the relationship, differentiated with respect to Snell's law,

$$I = \frac{P v_h \tan i_h}{x \cos i_o} \frac{d^2 t}{dx^2}$$

eq. 7

where, I is the energy density as defined by dE/dA, where E and A are Energy and Area of the wave front, respectively. P is the acoustic energy emitted per solid unit angle (dE/dΩ), v_h and i_h are the velocity and take-off angle at the focus and i_o is the incidence angle, [Udías, 1999]. Geometrical spreading corrections are therefore applied in the beginning of the processing sequence to account for the loss of seismic amplitudes which are inversely proportional to the depth to the reflection interface.

Amplitude corrections for physical attenuation of acoustic energy due to absorption by the medium through heat loss can also be done by applying a correction with the attenuation factor, Q. However, since water is considered a low-loss acoustic medium, Holbrook et al., [2003], physical attenuation corrections are not strictly necessary and do not significantly restore reflection amplitudes over geometrical spreading corrections alone.

2.3 SEISMIC REFLECTION IN OCEANOGRAPHY

Although acoustic probing of the ocean in various ways has been commonplace for decades, the first seismic reflection profiling in the ocean was done by Gonella and Michon, [1988] and Phillips and Dean, [1991]. These works, followed by the influential work by Holbrook et al., [2003] and subsequent studies (eg. Nandi et al. [2004]; Nakamura et al., [2006], Biescas, et al., [2008]), which have refined the seismic reflection "common mid-point" method to remotely image the ocean on a large scale (that is, to full ocean depths and horizontally on the order of 100's of km). While this method differs significantly over previous acoustic sounding experiments in its scale and method of implementation (see Section 4.2 for details), it also differs as a result of the acoustic frequency content used (bandwidths of 10 to several hundred Hz as opposed to kHz or MHz bands).

Scattering and reflection of acoustic waves is well-known to occur from biological sources, for

instance, zooplankton, [Stanton et al., 1996]. This factor must be considered when interpreting high frequency acoustic surveys. For example, Ross and Lueck, [2003] interpreted high frequency (300 kHz range) sound scattering as due to oceanic turbulence not due to zooplankton because they were able to independently estimate the quantity of zooplankton in the survey area from nets. However, seismic acoustic sources produce much lower frequencies and are not sensitive to structures as small as zooplankton. The data analyzed in Section 4 contain a frequency bandwidth of 10-90Hz. This corresponds to seismic wavelengths of between about 150 m and 17 m, respectively. Recalling the 1/4 wavelength approximation, we are thus able to image vertical thermohaline fine structure only as thin as about 4 m. Therefore we can be confident that zooplankton does not scatter seismic waves of these frequencies and thus is not a factor in the interpretation. The lower frequency seismic method complements conventional acoustic sounding experiments by imaging larger oceanic structures to greater depths (at the expense of the higher vertical resolution inherent in upper frequency bands) and complements conventional physical oceanographic logging by providing a view of the ocean at a lateral resolution of some two orders of magnitude finer (ie. 10 m compared to 1 km).

Reflected energy from an acoustic wave impinging on a boundary (half-space) is dependant upon the reflection coefficient (R) between the two media, [Yilmaz, 1987]. This is expressed as:

$$R = \frac{I_2 - I_1}{I_2 + I_1}$$

eq. 8

where I_1 and I_2 are the acoustic impedances of the respective media above and below the interface. Acoustic impedance in a fluid is the product of density and acoustic p-wave velocity (sound speed),

$$I = \rho v$$

eq. 9

where ρ is density and v is the sound speed of the respective media.

The magnitude of the reflection coefficient is thereby proportional to the contrasting physical properties of the media in question. In this way, water mass boundaries can be seismically 'mapped' by summing (stacking) seismic traces to generate a 2D 'snapshot' in space (horizontally, azimuthal to the acquisition path) and two-way acoustic travel time (vertically, corresponding to ocean depth). Two-way travel time is then converted to depth by multiplication by the sound speed.

Recent acquisition has been developed to confirm the correlation between acoustic impedance boundaries and temperature and/or salinity contrasts. Nandi et al., [2004] found that a close inspection

of seismic amplitudes revealed a direct relationship to the magnitudes of temperature contrasts. This method was successful in quantifying temperature variations across a boundary as small as 0.03°C. For vertical incidence plane waves, the reflection coefficient can be directly measured from the seismic section by the ratio of the reflected wave amplitude to the incident wave amplitude, [Yilmaz, 1987]. It is expressed as,

$$R=\frac{A_i}{A_0}$$

eq. 10

where $\mathbf{A_i}$ is the amplitude of the reflection in question and $\mathbf{A_o=-(A_{sf}^2)/A_{mult}}$, $\mathbf{A_{sf}}$ being the amplitude of the seafloor reflection and $\mathbf{A_{mult}}$ the amplitude of its first multiple, [Warner, 1990].

Whereas the magnitude of R of a boundary at a specific location identifies vertical (or near vertical) contrasts in physical properties between media, seismic coherency analogously describes horizontal contrasts in physical properties, coherence defined as a measure of the similarity of two or more functions, [Sheriff, 1991]. Specifically, seismic coherence measures the similarity of adjacent seismic traces, which form a reflection event. The principal method to distinguish among seismic events is the coherence between the individual traces of which it is comprised, [Sheriff, 1991]. Thus, strong, laterally continuous seismic events in the ocean are evidence of consistent boundaries between media with little variation in temperature and/or salinity contrasts. Páramo and Holbrook, [2005] found that variability of sound speed in water, more so than density is the dominant term controlling acoustic impedance, such that temperature and salinity may compensate one another in this way, [Rudnick and Ferrari, 1999]. That is, higher temperatures increase sound speed, but also decrease density, offsetting the sound speed increases. Furthermore, higher salinity values increase sound speed and density.

Some limits to the seismic method are manifest in its 2D nature and acquisition. One assumption is that the source generates a compressional plane wave that impinges on boundaries at normal incidence. However, data are only recorded in two spatial dimensions (azimuthally along the ship's course and in depth). Therefore, out-of-plane reflections or energy impinging on the receivers from offline are present. Furthermore, the term 'snapshot', in reference to a seismic profile should be used cautiously when applied to oceanography because of the dynamic nature of ocean currents relative to the time necessary for data acquisition. In a recent survey by the GO (Geophysical Oceanography) team in April-May, 2007 we found that fine details of thermohaline finestructure change notably on the order of as little as 3 hours (see Section 5). Thus, it is likely, particularly in areas of oceanic fronts and strong current velocities that the seismic section does not represent a true 'snapshot' in real time, but rather a picture of a progressively changing ocean along the line (figure 1, chapter 2).

3 – THE STUDY SETTING

3.1 - THE GULF OF CADIZ AND WESTERN IBERIAN COAST

The Gulf of Cadiz was chosen to test seismic reflection in oceanography for three principle reasons: 1) The strong oceanographic signature of the Mediterranean Outflow Water (MOW). Due to the penetration of the MOW into the North Atlantic through the Strait of Gibraltar, a strong identifiable contrast in salinity (between 36.35 and 36.65 psu) and thus, density (between 27.3 and 27.7 kg/m^3) is observed between the MOW and the surrounding Atlantic waters, [Baringer and Price, 1997]. Therefore, with density being one of the contributing factors to acoustic impedance (eq. 9), it is deemed a good potential target to test seismic reflectivity within the water column. 2) The large variety of oceanographic and topographic features, such as a continental slope, undulating seafloor (including seamounts and basins) and meso-scale Mediterranean eddy currents (Meddies), [Richardson et al., 2000]. These are believed to play an important role in maintaining the temperature and salinity distribution in the North Atlantic, [Bower et. al., 1997]. For this reason, testing seismic reflection in the Gulf of Cadiz provides more than just a curious search for water column reflections, but a natural laboratory to address actual oceanographic phenomena such as interaction with topography as well as characterization of mixing and entrainment processes. 3) Finally, extensive archived data sets of both oceanographic and seismic data allow interpretive constraints to be set and comparisons to be made between new and old data, thus enriching our knowledge of ocean processes in general.

3.2 - PHYSICAL OCEANOGRAPHIC RESEARCH IN THE GULF OF CADIZ

The Mediterranean Outflow Water has been comprehensively studied over the past several decades. Due to the high level of evaporation in the Mediterranean Sea its salinity and accordingly, its density, increase, [Richardson et al., 2000]. It then overflows through the shallow Strait of Gibraltar (300 m) as a density driven current and converts into an intermediate depth-jet, cascading down the continental slope and equilibrating at depths between 500 and 1500 m, meanwhile entraining the upper North Atlantic Central Water (NACW) and flowing as a westward guided current called the Mediterranean Undercurrent (eg. Heezen and Johnson, [1969]; Madelain, [1970]; Baringer and Price, [1997]; Bower et al., [2002]).

3.2.1 - PROBING THE OCEAN

The development of the CTD (Conductivity-Temperature-Depth) cast in 1955 led to accurate direct probing of the ocean and is still widely used, [Ingmanson and Wallace, 1995]. The CTD allowed the first direct Eulerian measurements of variation in physical properties with depth in the ocean by providing a measurement of salinity (conductivity), temperature and depth (pressure). Nowadays, expendable probes are more common because they allow an Eulerian measurement of physical ocean properties at fixed points in space as a function of depth and are deployable as the ship is moving. Thus, a much denser horizontal grid of data can be acquired with XBTs, whereas the CTD requires the ship to be stopped while it is lowered and raised. The Expendable Bathythermograph (XBT) is capable of measuring vertical resolutions as small as 65 cm and temperature variations as small as +/- 0.1 ºC, [Lockheed Martin Corp., XBT User's Manual, 2005]. The Gulf of Cadiz and the western Iberian coast have decades of historical XBT and CTD data at various locations. We draw upon these data to corroborate co-located seismic data.

3.2.2 - FLOAT MEASUREMENTS

In addition to in-situ Eulerian measurements of ocean properties, Lagrangian measurements, where a measuring device follows the trajectory within the fluid, are also informative. Beginning in 1993 (eg. Bower et al., [1997]), as part of the AMUSE (A Mediterranean Undercurrent Seeding Experiment) project, RAFOS floats were deployed and were tracked acoustically for 11 months. This experiment showed the path of Meddies and the Mediterranean Undercurrent and further established the significance of the undercurrent as having an important role in the broader Atlantic Ocean (figure 4).

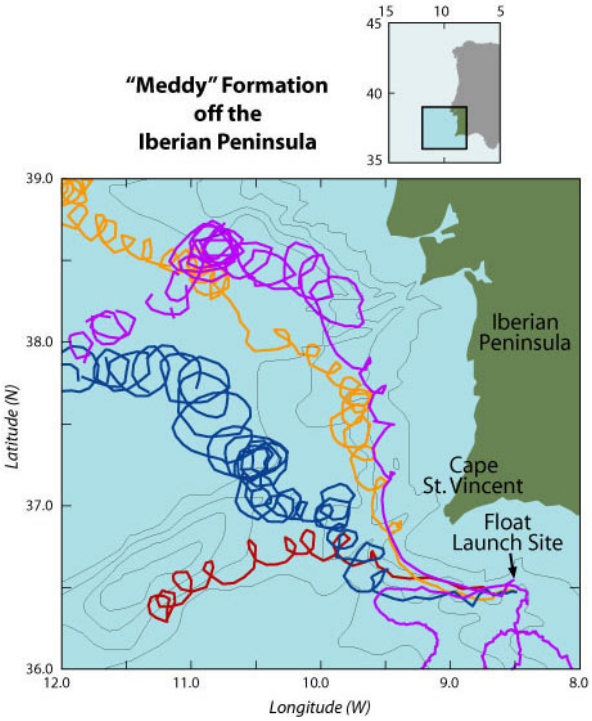

Figure 4 - Meddies tracked by RAFOS floats – courtesy, Jayne Doucette, Woods Hole Oceanographic Institution (used with permission)

To emphasize, Reid, [1979] has suggested that without the salinity contribution of the MOW the Norwegian-Greenland Sea cannot maintain its salinity and density having profound implications for the existence of the North Atlantic Deep Water (NADW). Likewise, Chan and Motoi, [2003] tested computer models of the MOW in a global perspective. They tested the possible effects of the MOW with and without exchanges of heat and salinity. They concluded that there would be a general decrease in salinity and temperature of surface waters in the Southern Ocean on a millennium time-scale, thus decreasing the Meridional Overturning Circulation that transports Antarctic Bottom Water (AABW). Chérubin et al., [2003] also observed that RAFOS floats can become trapped within the structure of a Meddy, a Mediterranean Water eddy, demonstrating the stability of these structures.

I build upon research into the characterization of physical oceanographic processes in the Gulf of Cadiz and western Iberian coast by analyzing seismic data and interpreting reflections in the context of interface stratification, turbulence, mixing and entrainment processes.

4 – MIXING AND ENTRAINMENT IN THE MEDITERRANEAN UNDERCURRENT

I demonstrate various seismic responses that correspond to different mixing regimes in the study area by analysis of marine seismic data from the Iberian-Atlantic Margin (IAM) survey acquired in 1993, which provide 2D images of the Mediterranean Undercurrent at four locations along its trajectory. I argue that seismic coherency (lateral reflection continuity) is a measure of the stability of isopycnal boundaries within the Mediterranean Undercurrent and between it and the surrounding Atlantic Waters (NACW and NADW). Outside the scope of this study are simultaneous temperature and salinity measurements that are needed for in-situ verification of the relationship between temperature and salinity variation and thermohaline fine structure in the study region, although recent, independent analyses provide confirmation of this relationship (eg. Nandi et al., [2004], Páramo and Holbrook, [2005], Nakamura et al., [2006]).

Seismic oceanography as a new scientific discipline opens up the potential to unlock decades of global seismic data keyed to the study of ocean dynamics. That is, re-processing and analysis of archived seismic data will add to the knowledge of ocean processes by allowing near real-time snapshot measurements (see Figure 1) of thermohaline stratification at different times and locations. This new and complementary remote sensing method advances understanding of geophysical fluid dynamic processes that are important to understanding the ocean.

The Mediterranean Undercurrent is an important hydrographic feature of the North Atlantic Mediterranean Water, which itself plays a significant role in global thermohaline circulation, [Reid 1979]. Mediterranean Water enters into the Atlantic Ocean through the Strait of Gibraltar as a result of the overflow of dense, saline water from the Mediterranean Sea, [Bower et al., 2002]. Guided by buoyancy and seafloor bathymetry it cascades downward into the Gulf of Cadiz and equilibrates at depths between 500 m - 1500 m, [Richardson et al., 2000]. Due to the Coriolis Effect, it acquires a northward component, [Ambar et al., 1999] and mixes considerably with the North Atlantic Central Water (NACW), [Johnson et al., 1994]. The northward flow then follows the west coast of Iberia into the Bay of Biscay, along the Porcupine Banks, all the while becoming more diluted, [Iorga and Lozier, 1999a]. By applying inverse methods to several sections in the gulf, Ochoa and Bray [1991] deduced that a pattern of entrainment and mixing is present. However this remains uncertain with hydrographic data alone, [Johnson et al., 1994]. Since the distinctive shape of the undercurrent was discovered, investigators have been trying to understand the processes that lead it from its source to the interior of the ocean, [Bower et al., 2002]. The multi-channel seismic reflection method (MCS) has been shown

to be well suited to analysis of the nature of oceanographic thermohaline fine structure (see Section 2.3), with lateral resolutions some two orders of magnitude greater than conventional oceanographic data. Specific studies by Holbrook and Fer, [2005] and Páramo and Holbrook, [2005] quantified internal wave energy and measured temperature contrasts inferred from AVO (amplitude-versus-offset) analysis, respectively, using seismic profiling. Seismic reflection profiling is unique in its application to oceanography because of its method of implementation. Its low frequency, yet high level of lateral sampling (horizontal resolution) allows oceanographers to create a snapshot in near-real time to better visualize isopycnal surfaces and internal waves over large distances, over frontal regions and continental slopes to improve upon ocean dynamic models (eg. Ruddick, [2003]; Thorpe, [2005]).

I analyze seismic data in combination with historical, co-located CTD data situated along the path of the northward component of the Mediterranean Undercurrent to characterize large-scale oceanic processes. I believe that areas of decreased lateral seismic coherency (broken reflectivity) imply they are regions of turbulence brought on by mixing through entrainment of surrounding waters masses.

Seismic analysis of the Mediterranean Undercurrent, specifically presents a unique opportunity to further corroborate the emerging seismic oceanography method because of the location of several seismic lines over a zone of oceanographic interest and the high temperature and salinity contrasts of the undercurrent relative to the surrounding Atlantic waters.

4.1 THE MEDITERRANEAN UNDERCURRENT

The Mediterranean Undercurrent carries Mediterranean Water from its source in the Strait of Gibraltar northward along the coast of Iberia. The undercurrent results from the channeling of Mediterranean Water (MW), [Madelain, 1970]. MW is distinct from the surrounding Atlantic Waters (NACW) because of its characteristically high salinity and temperature profile, [Ambar et al., 1999]. It has mean temperature and salinity values of 12°C, [Richardson et al, 1989], and 38.45 psu, [Xu et al., 2007], respectively. As the MW enters Portimão Canyon at the south coast of Portugal it makes the transition from a density driven current to an intermediate-depth jet due to quickly steepening topography and its associated turbulent entrainment, [Bower et al., 2002]. From Portimão Canyon to Cape St. Vincent a deeper, denser continuous stream of MW forms, [Bower et al., 2002]. This stream separates from the larger Mediterranean Outflow Water and is coerced northward by the Coriolis effect, where it may at times separate from the continental slope and generate large eddies (Meddies), which are low-potential vorticity structures which rotate anticyclonically, while preserving for long periods, the salinity and temperature characteristics of the MW, [Serra and Ambar, 2002]. The temperature and salinity contrasts between the Mediterranean Undercurrent and the NACW promotes entrainment of and mixing with the NACW. The upper core, being higher density entrains more NACW than the

lower core, [Serra and Ambar, 2002] as its volume transport then decreases northward, [Stephens and Marshall, 1999], thus trending toward homogeneity downstream. The Mediterranean Undercurrent follows the western coast of Europe, possibly as far north as the Porcupine Bank (50°N), although it is substantially diluted due to mixing at this point (eg. Daniault et al., [1994], Iorga and Lozier, [1999a]).

4.2 DATA ACQUISITION AND PROCESSING

4.2.1 Acquisition

The Iberian-Atlantic Margin (IAM) survey was carried out in August and September 1993 to study this tectonic plate boundary. The survey design and acquisition parameters used were customized to the study of deep crustal structures. Nonetheless, the high energy source and narrow receiver spacing used provide us with a rich seismic oceanography data set. Seismic profiles analyzed were chosen to intersect perpendicularly with the known path of the Mediterranean Undercurrent (figure 5) (eg. Richardson, [2000], Bower et al., [2002], Serra and Ambar, [2002]).

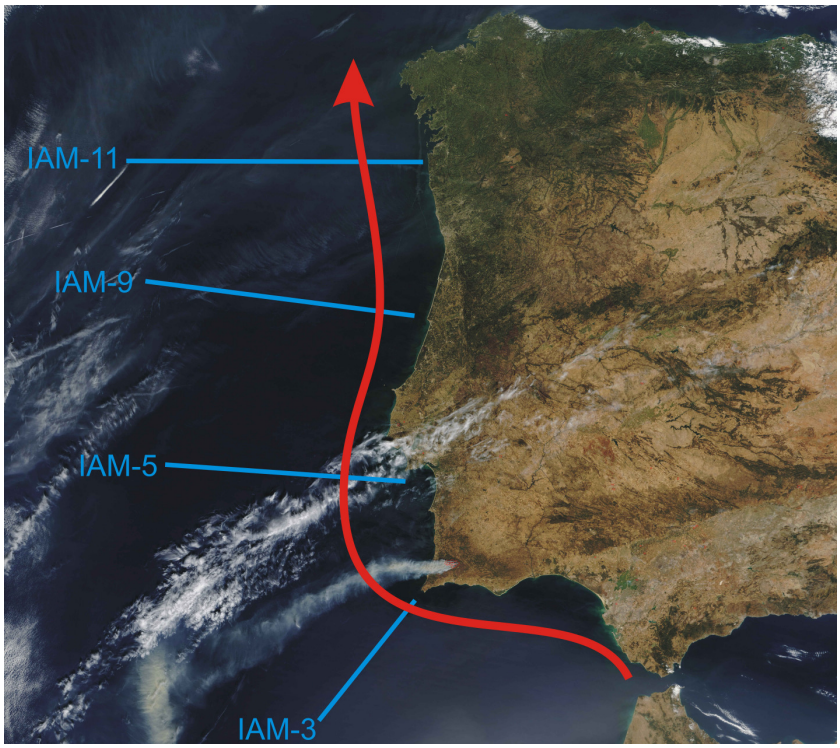

Figure 5 – location of analyzed seismic lines and the intersecting path of the Mediterranean Undercurrent. Note: the true width of the undercurrent is not illustrated.

Detailed acquisition parameters are summarized in Table 1. The streamer was the HSSQ/GX600 analog model and was 5 km long with 192 active channels, arranged in 25 m group spacings, giving a Common Midpoint (CMP) spacing (ie. lateral resolution) of 12.5 m. The streamer was towed at a

nominal depth of 15 m. The air gun array consisted of 36 BOLT guns organized into 6 identical sub strings and were towed at a nominal depth of 10 m (figure 6). The total volume of the air guns was 7524 cu. in. (123.3 L) and they were synchronized with ship speed to fire at 75 m intervals. The peak energy occurred in the frequency band of 20-50 Hz.

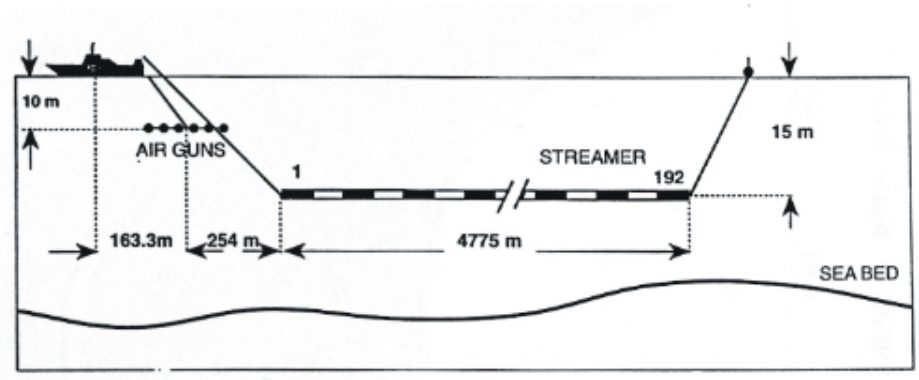

Figure 6 – Illustration of acquisition layout for IAM survey.

Acquisition Parameters	
Recorded by: Geco-Prakla, S/V GECO SIGMA, Aug-Sep, 1993	
ENERGY SOURCE type: SWAG airgun array (bolt) total volume: 7524 cu. in. source depth: 10 m shotpoint interval: 75 m	***INSTRUMENTATION*** type: DFS-V format: SEG-D sample rate: 4 ms record length: 25 s low cut filter: OUT high cut filter: 90 Hz (slope: 72 db/Octave)
CABLE CONFIGURATION number of groups: 192 group interval: 25 m cable depth: 15 m near offset (in-line): 254 m	***NAVIGATION*** primary: DGPS secondary: Transit

TABLE 1 – IAM ACQUISTION PARAMETERS

4.2.2 Processing – direct wave suppression

One of the challenges in seismic processing of data from the oceans is sufficient suppression of the direct wave. The direct wave is the seismic energy that travels directly from source to receiver without reflecting. Normally, the entire water column is muted from seismic data along with the direct wave, for crustal studies. However, the direct wave masks water column reflections as high amplitude linear noise. Hence, it needs to be suppressed while minimally affecting reflected energy before standard

processing modules are applied. The suppression of the direct wave was carried out using the Eigenvector filter module. This filter, based on the Kahrunen-Loeve theory, [Jones and Levy, 1987], decomposes the seismic traces into eigenimages. That is, characteristically different functions via eigenvectors. Flattened events are subtracted after filtering through the chosen eigenimage. Therefore, to suppress the direct wave, the shot record is first flattened using a linear moveout correction (LMO) with a constant water velocity of 1505 m/s, the eigenvector filter is applied and the LMO correction reversed (figure 7).

It is evident from figure 7 that after application of the filter, clear reflections are revealed, which were previously masked. The Eigenvector filter proved less effective at removing near offset traces of the direct wave. Therefore, offsets were then limited to between to 700 m (where the Eigenvector filter becomes largely effective) to 5029 m (maximum offset). The high fold (redundancy) of the multi-channel seismic method compensates for these limited offsets somewhat. However, high-frequency energy (and therefore, resolution) is invariably diminished at longer offsets due to elastic wave attenuation. Hence, higher resolution is sacrificed by not including near traces. Other, untested methods, may be preferable to remove the direct wave without truncating near offset traces. The Tau-P filter was tested with similar results for near-offset traces. Before applying the Eigenvector filter, shot gathers were carefully analyzed to choose the most effective windowing and frequency parameters.

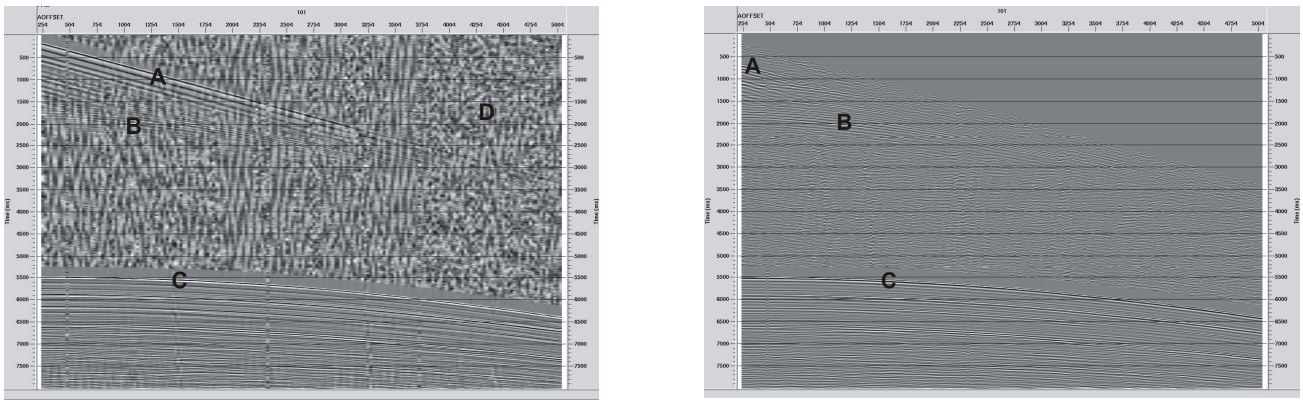

Figure 7 – Typical shot record from one IAM profile (IAM-3 – SHOT 101) showing seismic events. **A**: Direct wave; **B**: Water column reflections; **C**: Seafloor reflections; **D**: Random noise. The shot record on the left shows the high amplitude direct wave that masks weak water column reflections as well as significant random noise. After application of the Eigenvector filter, the direct wave is largely suppressed, with the exception of some residual energy at near offsets. The Eigenvector filter was also very effective in removing the random noise.

4.2.3 Processing – step-by-step

The Iberian-Atlantic Margin lines were processed using ProMAX v.2003, Seismic Unix and Claritas 4.4.1 software. All lines were processed similarly, with the exception of particular dataset dependant parameters. This was to ensure consistent interpretation from line to line. See Appendix 1 for processing details.

The first stage of processing involved the application of marine geometry to the trace headers. During acquisition, geographical positioning data collected from satellite and seismic acquisition parameters are written to disc. Correct geometry definition is important because the correct spatial location of shots and receivers and the source-receiver offset of individual traces needs to be known to be able to create veritably referenced CMP stacked traces. Next, the direct wave suppression was carried out (see previous section). Then an Ormsby band-pass filter was applied, truncating the frequency range from 15 to 90 Hz, with tapered ends (8/15 – 90/100 Hz), to prevent discontinuities such as oscillatory edge effects.

Next, a correction for spherical divergence energy loss was applied that operates on the basis of a 1/distance relationship. Velocity was not treated as spatially or temporally variable since sound speed in water varies minimally. A single trace scalar called Ensemble Balance was executed to balance trace amplitudes for display purposes. Ensemble Balance scales all samples in a trace by the same scalar, as opposed to Automatic Gain Control (AGC), which scales based on a sliding time window. In this way, lateral variations in amplitude are better preserved. However, for true amplitude analysis (section 4.4), no trace gain was used.

Velocity Analysis was done on CMP gathers starting with a constant velocity of 1505 m/s. Careful analysis of semblance spectra and NMO event flattening of the gather (figure 3, chapter 2) shows that water stacking velocity varies between about 1480 m/s and 1550 m/s. Visual stack comparisons before and after velocity analysis do display a marked improvement, especially in the shallow ocean (0-600 m), figure 8.

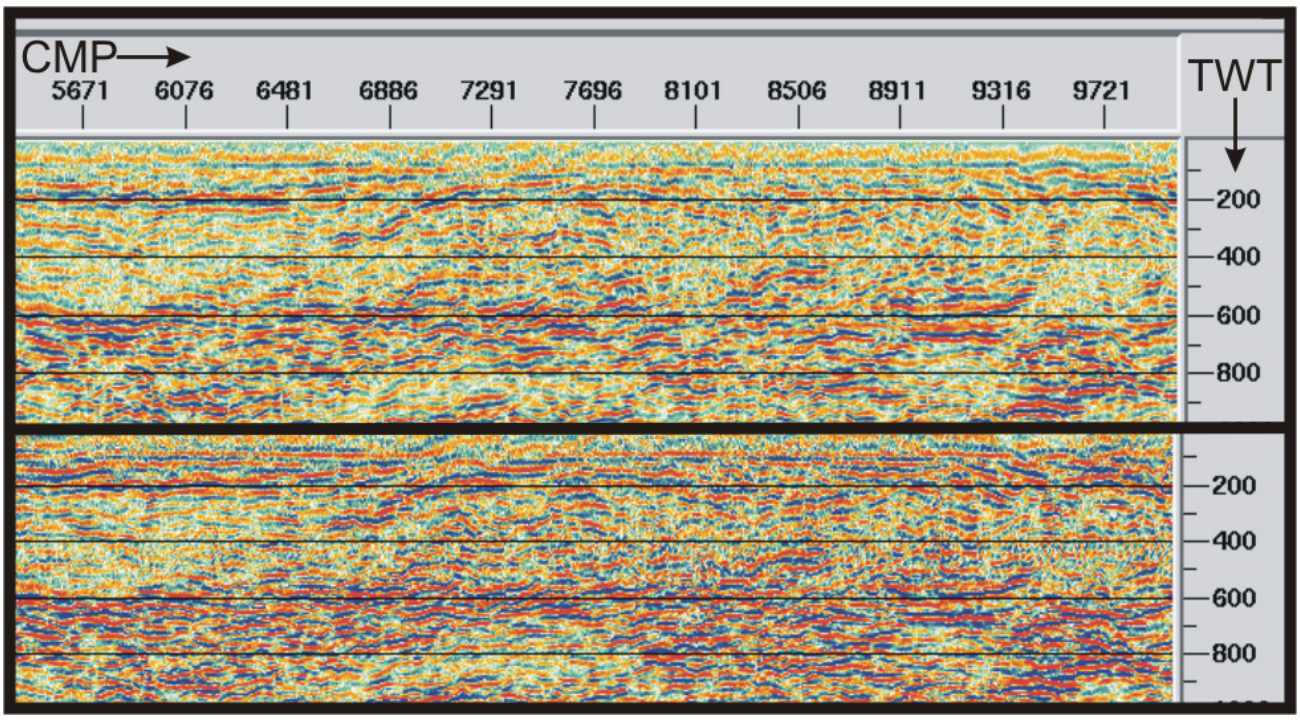

Figure 8 – Comparative results of semblance velocity analysis for line IAM-3. Upper panel stacked with a constant velocity of 1505 m/s. Lower panel stacked using a carefully picked temporally and spatially varying velocity function. Note the generally clearer reflections and subtle structural changes. Horizontal axis is common midpoint (CMP) and vertical axis is two-way time (TWT).

After velocity analysis, common midpoints were NMO corrected and stacked to generate CMP stacked profiles (section 2.2.7). Traces were summed based on the mean vertical stacking algorithm that sums each of the sample values and divides by the square root of the total number of samples summed.

Post-stack processing included a f-x deconvolution to improve signal-to-noise ratio. This proceeded by Fourier analysis into the frequency (f) - distance (x) domain from the time – distance domain and applied a wiener prediction filter to each specified frequency. The output traces therefore have significantly lower noise.

Finally, a phase-shift time migration was applied to move reflectors to their true spatial locations and to collapse diffractions. Some migration artifacts were introduced from the high amplitude sea floor reflections into the deep ocean. Currently, several different pre-stack time and depth migrations are being testing to help minimize this effect. For the display stacks in section 4.3, Automatic Gain Control was applied over the complete trace length to enhance display amplitudes against the dominant seafloor reflections. For true amplitude analysis, this was not applied. Two-way time profiles were converted to depth using the interval velocity function, derived from chosen stacking velocities via the Dix equation.

4.3 – RESULTS

A comparison of the four seismic lines (figure 5, chapter 4) and geographically coincident oceanographic temperature and salinity in-situ measurements from CTD casts shows the behavior of the Mediterranean Undercurrent proceeding north The Mediterranean Undercurrent is shown in cross-section by these seismic lines, the undercurrent moving Northwest, then North, perpendicularly into the plane of the figures. Bearing in mind that the seismic reflectivity of water mass boundary interfaces depends directly on contrasts in the respective physical water properties, namely temperature and salinity, we propose our interpretation.

Based on previous oceanographic studies (see section 4.1) and on relative seismic amplitudes we interpret the reflections from surface to approximately 600 m as the North Atlantic Central Water (NACW), from about 600 m to approximately 1800 m depth as Mediterranean Water (MW) and from 1800 m depth to the ocean floor as the North Atlantic Deep Water (NADW). Consistently, reflectivity in the MW is more prominently visible throughout the sections, with the NACW and NADW showing less reflectivity.

In general, the oceanographic data show decreasing salinity and, much less so, decreasing temperature along the path of the Mediterranean Undercurrent. Accordingly, the seismic horizontal coherency decreases upstream in places, however it remains locally coherent in others.

Temperature and salinity both influence density and sound speed values, therefore affecting acoustic impedance and likewise reflection coefficient, but a theoretical relationship between them is not clear at this time. However, recent work by Sallàres, [2008] on a Geophysical Oceanography (GO) data set (Section 5) from the Gulf of Cadiz (2007) addresses the relative proportions of temperature and salinity to reflection coefficient (figure 9).

In this study, temperature is found to be the dominant influence, but the salinity contribution is also significant (some 30%). Given these results, in regimes where temperature variations are small, salinity may have a more important influence on reflection coefficient. For the historical oceanographic dataset corresponding to the location of the IAM lines, temperature variations between the lines are small. This indicates that for the Mediterranean Undercurrent, salinity may be a more significant factor for reflection coefficient.

It is well known that temperature diffusion occurs more rapidly than salt diffusion by a factor of about 100 (eg. Stern, [1960]; Ruddick, [1992]). Therefore, along the path of the undercurrent, temperature should equilibrate quickly, whereas salinity will persist for longer times, giving rise to reflection coefficient contrasts further downstream (NW Iberia) that are in a larger part due to salinity. Nonetheless, further study is needed to establish a firmer relationship between temperature and salinity contributions to reflection coefficient and how much they may vary from location to location or with

changing conditions.

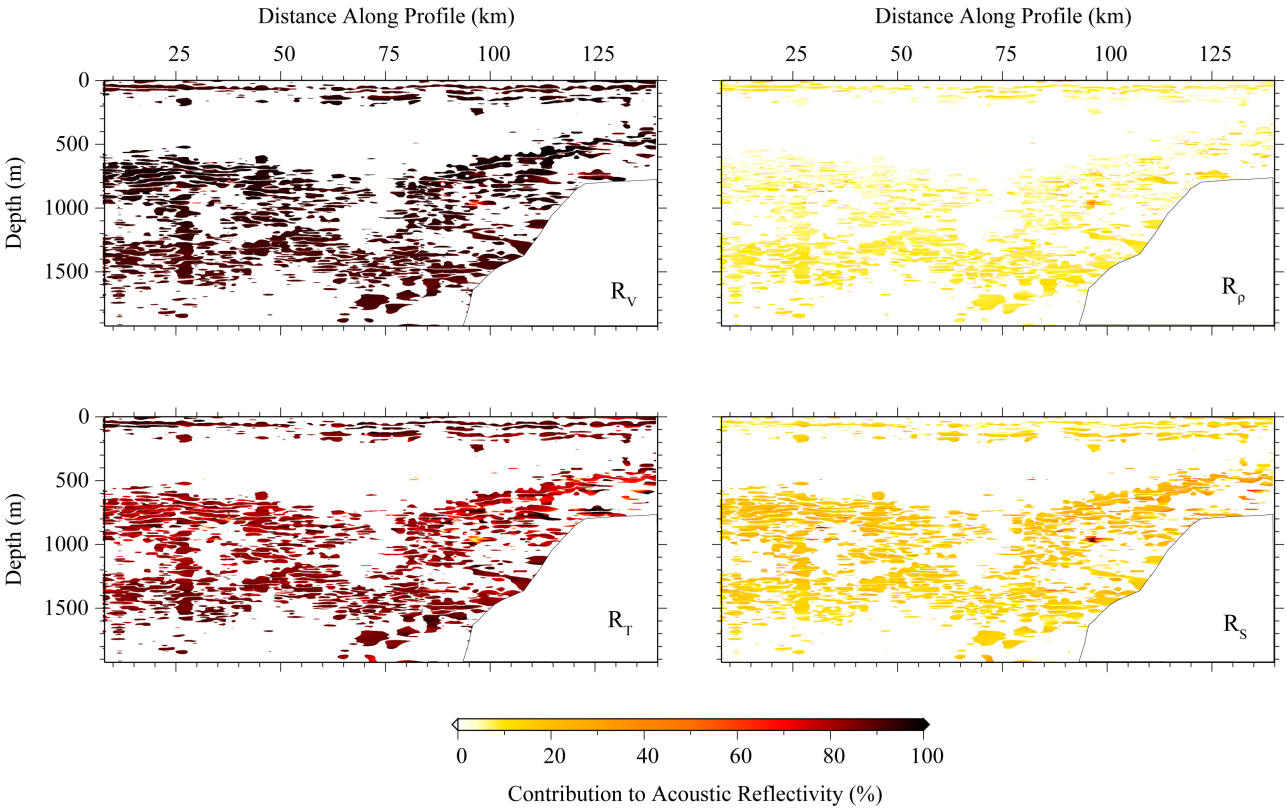

Figure 9 – Contributions to acoustic reflectivity from (clockwise from top left): sound speed (V), density (ρ), salinity (S) and temperature (T). Clearly, in this region of the Gulf of Cadiz (nearly coincident with line IAM-3) sound speed is the dominant factor, followed by temperature, salinity and density. Since temperature and salinity affect both density and sound speed to various degrees, this empirical relationship is not absolute, but may vary from location to location. The contribution of salinity in this case is about 30-40%. Data are from GO cruise, April-May, 2007. (Sallàres, 2008).

4.3.1 - IAM-3

The seismic section in figure 10 (and Appendix 2, Panel A) is line IAM-3, a SW-NE direction line (see figure inset). Across the image is strong horizontal and sub-horizontal stratification. This corresponds very well with the corresponding abrupt oceanographic changes in temperature and salinity at these depths, as well as published oceanographic measurements that identify the Mediterranean Water, [Richardson et al., 2000]. The stronger seismic reflections near the bottom of the Mediterranean Water are interpreted to be the beginning of the ocean abyssal water (NADW).

We identify the prominent lens shaped structure as a Meddy because it contains two distinct cores, [Bower et al., 1997], is located at the depths 500-1500 m predicted by CTD and float surveys, [Armi et al., 1989] and [Richardson et al., 1989] and shows strong reflection continuity, indicating that it is relatively stable, [Chérubin et al., 2003], as opposed to turbulent or chaotic. Furthermore, it intrudes into and distorts the lower laminar stratification of the Mediterranean Water/NADW boundary,

which suggests rotation and mixing is occurring.

The dipping structure may be a sinking saline plume, which penetrates below the Mediterranean Water as it mixes with and entrains horizontal laminar stratification. The mixing and entrainment cause the descending plume to approach neutral buoyancy as it begins to settle and stratify somewhat. The reduction in seismic coherency within the dipping plume also indicates a lowering in density and/or sound speed (acoustic impedance) contrasts, which imply mixing and therefore increasing homogeneity.

The north-east side of IAM-3 displays strong lateral reflection continuity but also shows dipping events and zones of low lateral coherency. This indicates lower relative temperature or salinity contrasts, which imply more homogeneous water mass boundaries, perhaps as a result of the water's interaction with the continental shelf. Notable here is a half lens-shaped structure which may suggest the formation of a Meddy at Cape St. Vincent (eg. Serra and Ambar, [2002]).

In general, seismic amplitude contrasts between the NACW and the MW are smaller than between the MW and the NADW. This suggests that more mixing has occurred between the NACW and the MW than between the MW and NADW due to entrainment of NACW, [Bower, et al., 2002], thus increasing its homogeneity. At the top of the Meddy, however, there is a stronger than average amplitude contrast. This agrees with studies that indicate higher density contrasts at the top of Meddies promote more entrainment of NACW, (eg. Serra and Ambar, [2002]; Biescas et al., [2008]).

The temperature profile of IAM-3 shows surface temperatures of about 17° or 18° and within the NACW, grading to 10° to 14° in the MW and dropping abruptly to below 5° in the NADW. Its salinity values range from about 36.5 psu at the surface, dropping to near 35.5 psu at 300 m depth, then increasing again to between 36 psu and even exceeding 36.5 psu from 500 m to 1600 m, then decreasing to about 35.5 psu until 1800 m, then dropping to 35.2 psu until 2100 m and finally decreasing to below 35 psu below 2100 m.

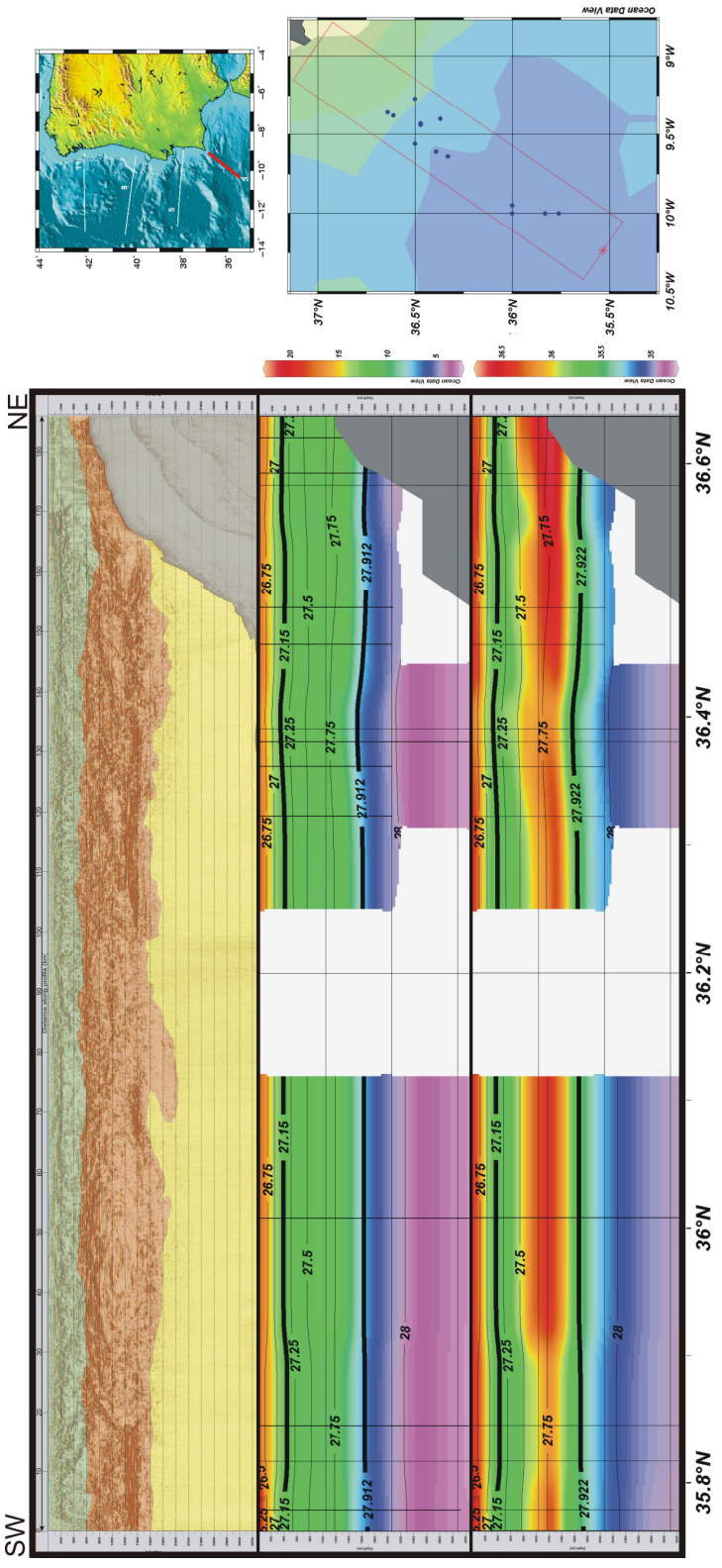

Figure 10 – co-located seismic (line IAM-3) and historical oceanographic data showing agreement between three principal water masses. Seismic water masses are defined based on degree of reflectivity (top panel). Water masses according to oceanographic data are defined by temperature (middle panel) and salinity (lower panel), respectively. For this line, temperature stratification is stable, whereas there is a high salinity anomaly. Black lines in oceanographic data correspond to neutral density isopycnals (kg/m^3). Oceanographic data plotted with Ocean Data View. Vertical exaggeration: 13.

4.3.2 – IAM-5

Line IAM-5 is an E-W oriented line, north of IAM-3, figure 11 (and Appendix 2, Panel B). Based on amplitude contrasts alone, it images the Mediterranean Undercurrent between approximately 400 m and 1600 m and shows high lateral coherency, especially in the eastern part.

Curiously, in the most western section there is a distorted lens-like structure with two apparent cores. Oceanographic float experiments (eg. Richardson, et al., [2000]; Bower et al., [2002]; Serra and Ambar, [2002]) performed in the Gulf of Cadiz show meddies translate westward near the location of line IAM-5 due to slope topography, suggesting that this structure may represent some transect through a part of a Meddy. The eastern third of the seismic section exhibits much more lateral continuity than the west with some interesting events that dip toward the continental shelf. Given that the undercurrent turns north at Cape St. Vincent and therefore loses energy due to its westward inertia, this stable stratification seems to indicate a zone of low turbulence resulting from the overshoot of the undercurrent around the continental shelf, allowing the density stratification to form.

The temperature profile of IAM-5 displays surface temperatures of about 17° dropping gently to about 15° in the NACW, then grading to 10° to 14° within the MW and dropping below 5° in the NADW. Its salinity values range from about 36.3 psu at the surface, dropping to near 35.6 psu at 200 m depth, then increasing to a maximum of 36.4 psu from 600 m to 1600 m, then decreasing to about 35.6 psu until 1800 m, dropping to 35.2 psu until about 2000 m and finally falling below 35 psu below a depth of 2100 m. Compared to IAM-3, the salinity profile has decreased somewhat.

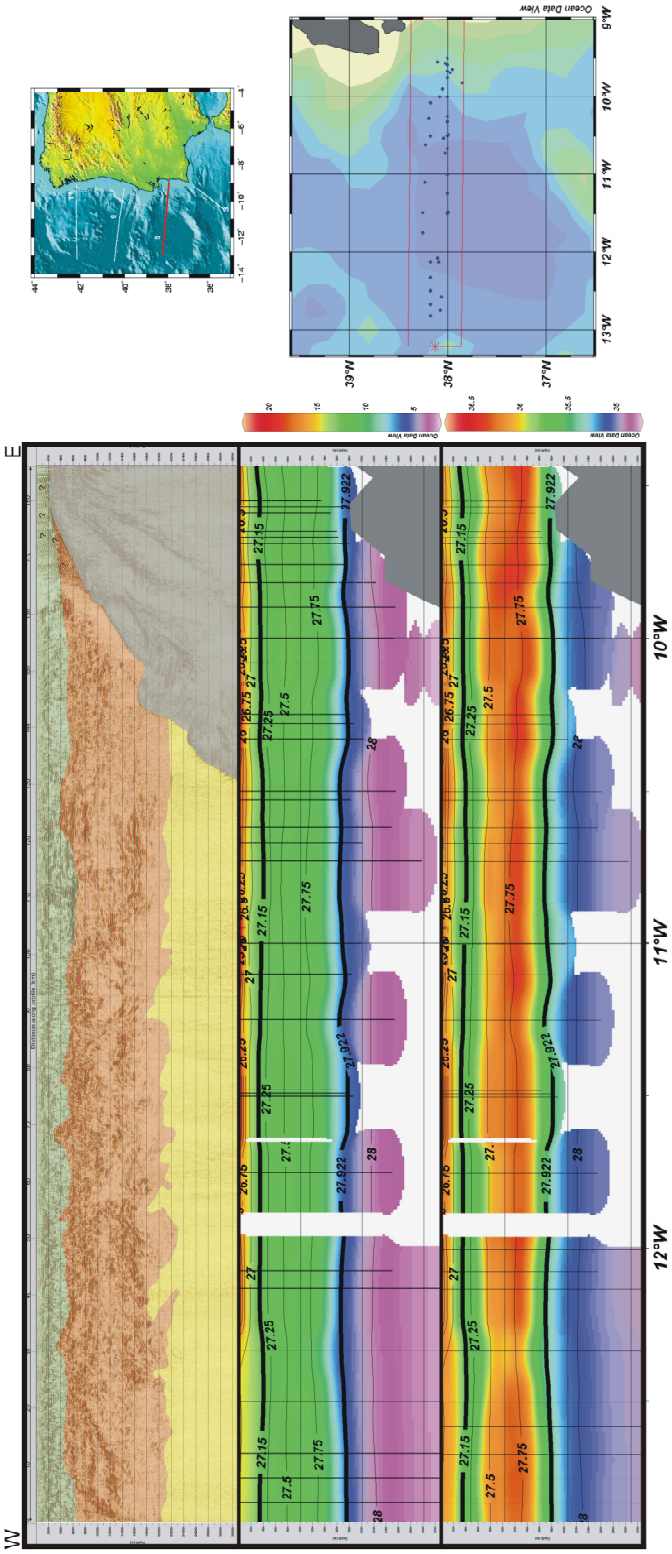

Figure 11 – co-located seismic (line IAM-5) and historical oceanographic data showing agreement between three principal water masses. Seismic water masses are defined based on degree of reflectivity (top panel). Water masses according to oceanographic data are defined by temperature (middle panel) and salinity (lower panel), respectively. Temperature stratification is still relatively stable and high salinity anomaly begins to decrease, indicating dilution. Seismic horizontal coherency has decreases. Black lines in oceanographic data correspond to neutral density isopycnals (kg/m^3). Oceanographic data plotted with Ocean Data View. Vertical exaggeration: 13.

4.3.3 – IAM-9

Moving northward along the coast of Iberia and along the trajectory of the Mediterranean Undercurrent, figure 12 (and Appendix 2, Panel C) we observe more broken thermohaline fine structure. This seems to suggest that in some areas there is turbulence brought on by mixing that prevents the formation of laminar stratification. However, the undercurrent is still well defined between 400 and 1600 m depth and at some parts of the line shows a sharp transition from strong reflectivity to transparency over just 200 m depth (1600 to 1800 m). But on the whole it is less laterally coherent than IAM-3 or IAM-5, both of which show very smooth laminarity. The westernmost part of the line shows more seismic transparency from the surface to about 1000 m depth and suggests a well-mixed, homogeneous zone. From 1000 m to the base of the Mediterranean Water reflectivity increases and includes some eastward dipping structures which penetrate below it. This may be as result of a negatively buoyant salt plume, that is, a high density anomaly, similar to the one seen in IAM-3. Moving east toward the coast of Iberia there are some relatively transparent zones over well stratified layers. Particularly, at km 69 there is a pronounced decrease in reflectivity between 600 and 1200 m depth. More to the east of this, stratification increases from the surface to the base of the Mediterranean Water from 106 to 203 km. Within this large zone, there is notable continuous stratification at the base with high seismic coherency and some plunging structures above showing internal structure. Stratification then becomes less prominent as the line approaches the continental slope.

The temperatures for IAM-9 in the upper 150 m are about 17° dropping quickly to about 14° before 200 m, corresponding to the NACW. The temperature then remains in the to 12° to 14° range corresponding to the MW, until about 1500 m, and dropping sharply to below 5° from 1500 m to 2000 m, representing the NADW. Salinity values range from about 36.0 psu at the surface, dropping to about 35.6 psu at 200 m depth, then increasing to between 36.1 psu and 36.3 psu from 700 m to 1600 m, with a notable salinity anomaly near the western part of the line. Salinity values then decrease to between 35.5 psu and 35.3 psu until 1800 m, dropping to 35.2 psu until about 2100 m and finally dropping to below 35 psu below 2100 m. Generally, the salinity values have dropped significantly compared to IAM-3 and IAM-5.

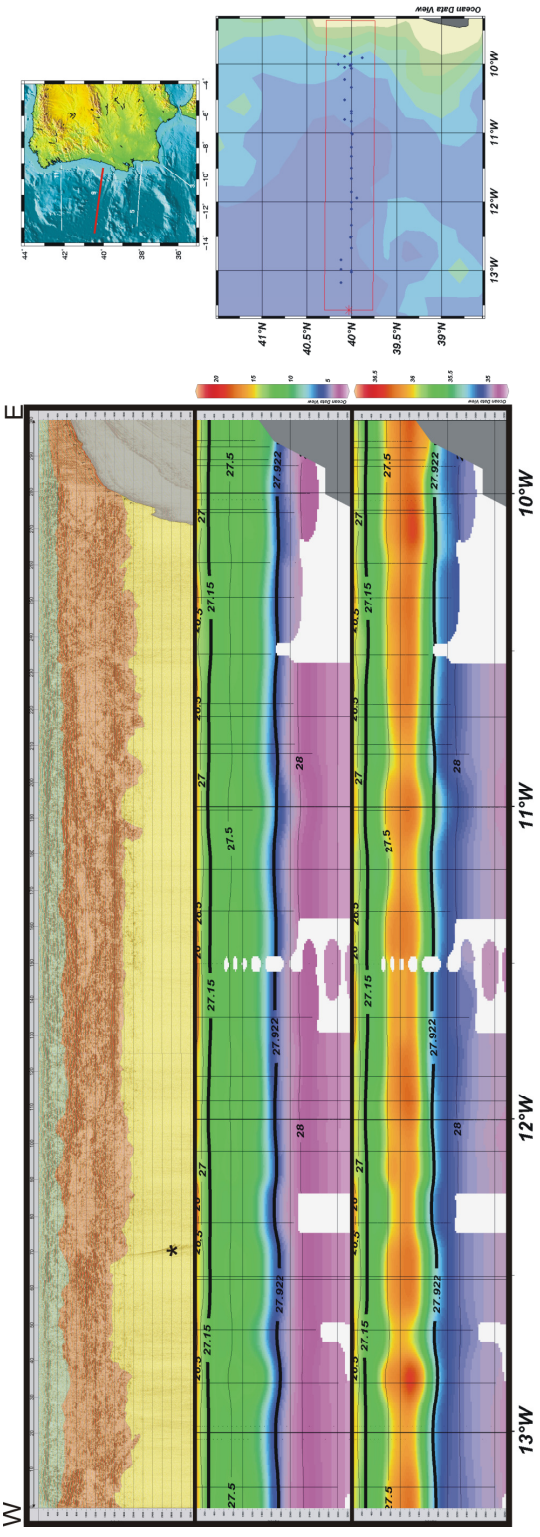

Figure 12 – co-located seismic (line IAM-9) and historical oceanographic data showing agreement between three principal water masses. Seismic water masses are defined based on degree of reflectivity (top panel). Water masses according to oceanographic data are defined by temperature (middle panel) and salinity (lower panel), respectively. Temperature stratification remains consistent with previous lines. Salinity anomaly has decreased. Seismic data show some strong horizontal coherency, but also areas of broken reflections, especially near the continental shelf. Black lines in oceanographic data correspond to neutral density isopycnals (kg/m^3). Oceanographic data plotted with Ocean Data View. * represents seismic artifact. Vertical exaggeration: 13.

4.3.4 – IAM-11

The northernmost line studied, figure 13 (and Appendix 2, Panel D) shows the same zone of Mediterranean Water between 500 and 1500 m depth, but is less horizontally continuous than the other lines. The westernmost portion of the line, which is over the deepest part of the section is more broken, suggesting turbulence. There is a large lens-shaped structure from km 48 to 82, which I suggest could be a Meddy based on its dimensions matching other studied Meddies (eg. IAM3), [Richardson et al., 2000]. Curiously, unlike the Meddy from line IAM-3, it contains little internal structure. This indicate Meddies becoming more well-mixed internally as they evolve, resulting in converging salinity contrasts and hence, lower acoustic impedance contrasts. The corresponding salinity profile (bottom panel) also shows a large, near-constant salinity anomaly (about 36.3 psu – within the range typical of Meddies, [Richardson et al., 2000] near the western edge of the line, having roughly the same dimensions. They therefore, may be the result of related processes. However, since the seismic and oceanographic data were not recorded simultaneously, we cannot confirm this, although, it does support the observation that large salt lenses can persist some distance from the source of the Mediterranean Water, [Richardson et al., 2000]. The seismic data do show a seismically transparent lens, which could suggest near-constant internal salinity, given the narrow interior temperature range in the MW observed between 12° and 14°. The eastern part of this line shows low lateral coherency, indicating turbulent conditions are present, especially along the boundary with the NADW. This implies further mixing and dilution than the southern lines.

The surface temperature ranges for IAM-11 are about 13° to 15° dropping smoothly to 1400 m with slightly warmer values near the continental shelf. The NACW and MW, here have approximately the same temperature ranges, which we expect because of the latter entraining and mixing with the former and thus approaching thermal equilibrium, farther from the MW source. Yet, salinity contrasts still remain, albeit diminished. The temperature remains in the 12° to 14° range then drops sharply to below 5° from 1600 m to 1900 m, representing the NADW. Salinity values range from about 35.7 psu to 35.9 psu at the surface, dropping to about 35.6 psu at 800 m depth. Salinity then increases to between 36.0 psu and 36.2 psu from 800 m to 1500 m, with an isolated salinity anomaly near the western part of the line of about 36.3 psu, characteristic of Meddies, [Richardson et al., 2000]. Salinity values then decrease to between 35.5 psu by 1700 m, degrading quickly to 35.2 psu until about 1900 m and finally dropping under 35 psu below 1900 m depth. Compared with IAM-3, 5 and 9, the salinity content corresponding to the location of IAM-11 is much less. This implies that, given the faster approach to thermal equilibrium than salinity equilibrium, perhaps for the more northern lines, salinity has a more significant contribution to acoustic impedance.

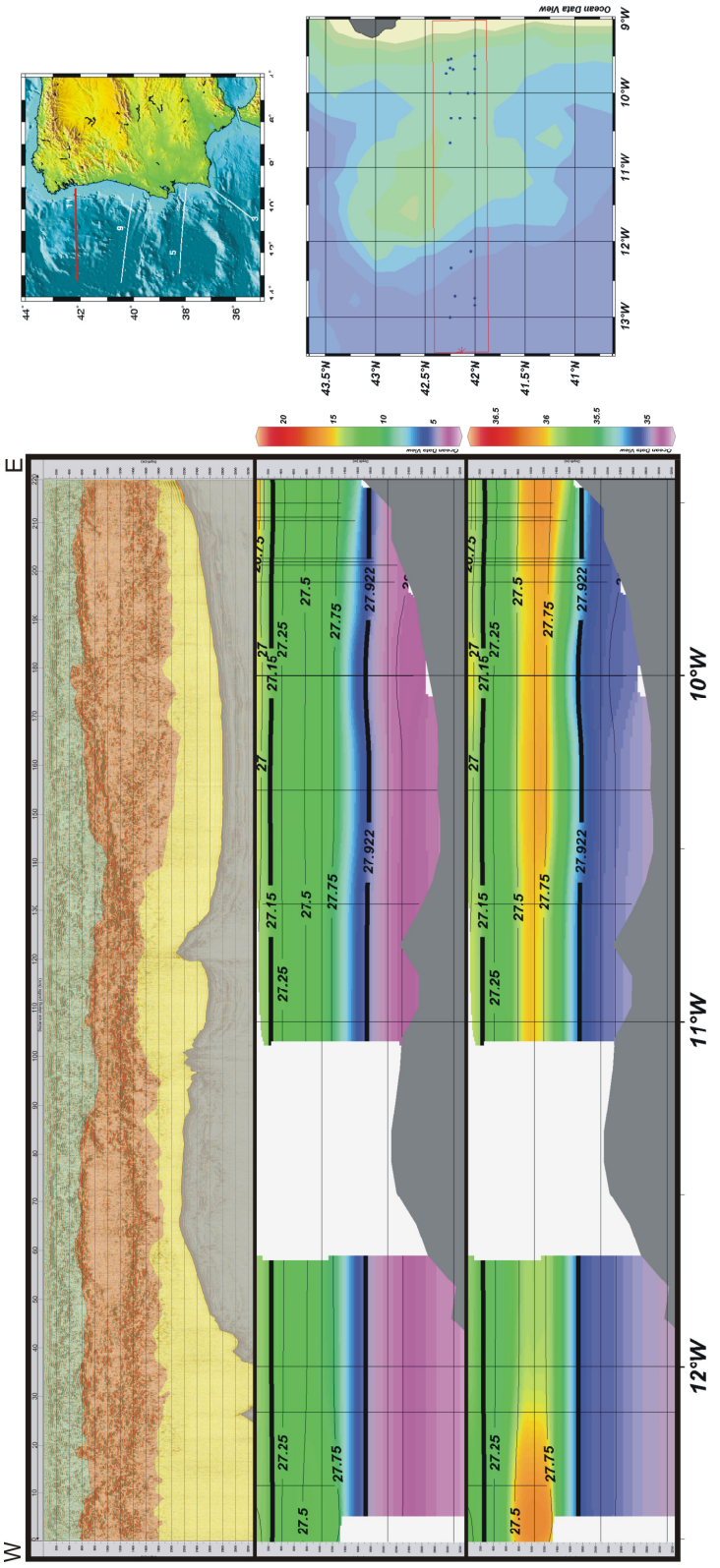

Figure 13 – co-located seismic (line IAM-11) and historical oceanographic data showing agreement between three principal water masses. Seismic water masses are defined based on degree of reflectivity (top panel). Water masses according to oceanographic data are defined by temperature (middle panel) and salinity (lower panel), respectively. Temperature stratification again remains stable, whereas salinity anomaly has marked been reduced. Some strong reflectivity, but low horizontal coherency, especially towards the east. Black lines in oceanographic data correspond to neutral density isopycnals (kg/m^3). Oceanographic data plotted with Ocean Data View. Vertical exaggeration: 13.

4.4 – TRUE AMPLITUDE ANALYSIS

In order to understand the quantitative relationships between the oceanic physical characteristics that influence reflectivity it is necessary to analyze true seismic amplitudes. Seismic lines shown in section 4.3 and Appendix 2 all are displayed with trace scaling, which applies a scalar to amplitude values. A trace balance processing module was selected to preserve lateral amplitude variations, however amplitude contrasts between the seafloor and those internal to the water column are prominent, so vertical trace balancing partially distorts relative amplitudes.

Complex trace analysis allows two ways of quantifying amplitude relationships. The amplitude of an envelope (erroneously, but more commonly referred to as 'instantaneous amplitude') of a time series is equal to the reflection strength, [Sheriff, 1991]. This is calculated by the Hilbert Transform, [Claerbout, 1976]. Analysis of reflection strength on the IAM lines shows moderate reflectivity in the upper ocean, approximately 0 - 700 m, high reflectivity from approximately 700 m to 1500 m, grading to very low reflectivity from 1600 m to the seafloor (figure 14). The oceanographic data show a minimally varying temperature profile in what corresponds to the Mediterranean Water, but a distinct salinity anomaly. Thus, salinity contrasts may therefore play a more significant role in influencing the high reflectivity of the Mediterranean Water. This could especially significant further downstream, contrary to results in the Gulf of Cadiz by Sallàres [2008] (figure 9) that show only a 30% contribution from salinity to reflectivity coefficient.

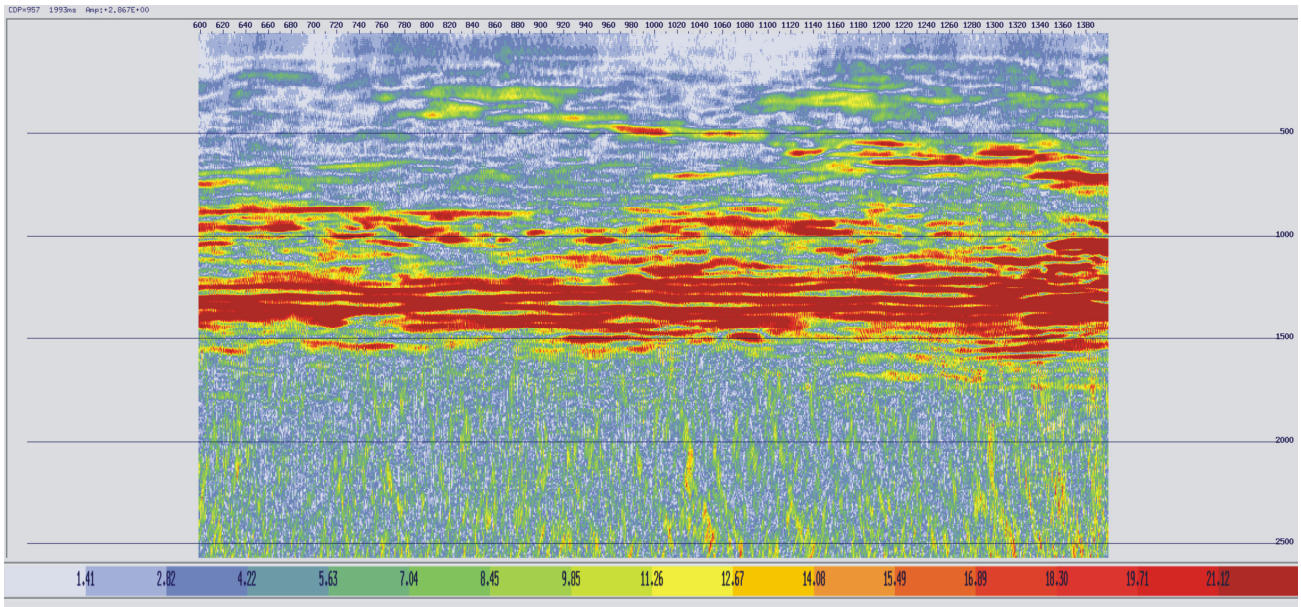

Figure 14 – plot of reflection strength for line IAM-3. Higher reflectivity is in red, lower reflectivity in blue. Note moderate reflectivity in the upper 800 m of the ocean, corresponding to the NACW, very high reflectivity from 900 m to 1600 m, corresponding to the MW, and low reflectivity values in the abyssal ocean, or NADW. Sub-vertical moderate reflectivity in NADW are noise artifacts from high amplitude seafloor reflections.

Analysis of average absolute amplitude on non-gained data shows the large contrast in relative amplitudes from reflections in each of the identified water masses. Reflections from the North Atlantic waters have significantly lower amplitudes (typically, half) than those of the Mediterranean Water, figure 15. For these results, I expected higher values for the MW, as shown, but also significantly lower amplitude values for the NADW than even the NACW, due to the fact that the NADW is known to be more well-mixed, therefore more homogeneous, resulting in less reflectivity. The fact that this is not illustrated in the analysis below may be due to several possible factors: 1) the most likely case, that the high amplitude seafloor reflection artifacts are contaminating the NADW. I will attempt to resolve this presently by muting the seafloor reflections for true amplitude analysis; 2) that amplitude analysis windows were picked erroneously; or 3) that there really is rather strong reflectivity in the NADW, although independent oceanographic studies contradict this possibility, [eg. Munk and Wunsch, 1998].

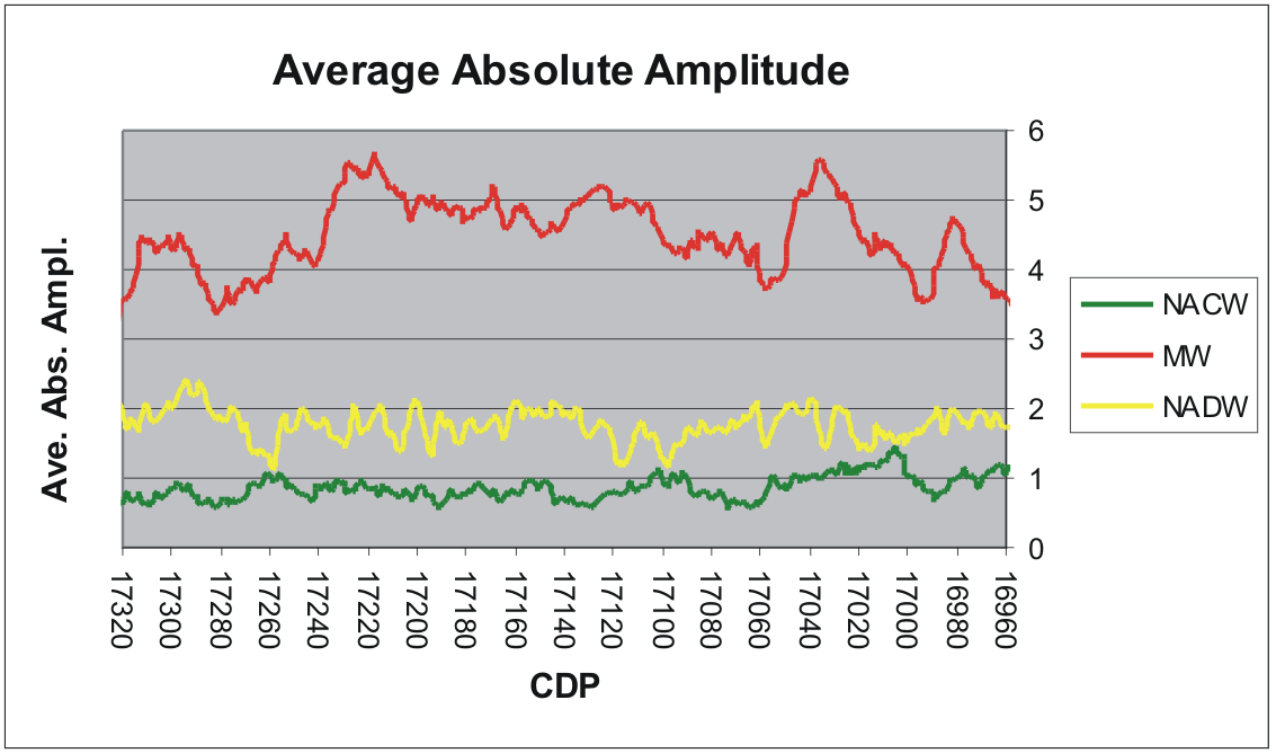

Figure 15 – Plot of average absolute amplitudes for a representative section of line IAM-11. NACW: North Atlantic Central Water; MW: Mediterranean Water; NADW: North Atlantic Deep Water.

4.5 – DISCUSSION

Analysis of four seismic lines acquired in August and September, 1993 as part of the Iberian-Atlantic Margin survey, which transect the Mediterranean Undercurrent show distinct thermohaline stratification in the upper 1800 m of the ocean. Layering is most prominent from approximately 500 to 1500 m, corresponding to the MW, though this varies somewhat from line to line. Common to all sections is the sharp negative seismic reflectivity gradient between 1400 m and approximately 1800 m, which we interpret as the base of the Mediterranean Water. This may suggest that abyssal water in the region of study is largely homogeneous in terms its thermohaline structure and therefore, is relatively more transparent to seismic waves than boundaries in the upper ocean (figure 14).

Reflectivity in the NADW is generally low, with the exception of some plunging structures that penetrate the lower seismic boundary of the MW such as is prominently displayed in line IAM-3 and in the western edge of IAM-9 and what are likely seafloor reflection artifacts (see previous section). Several instances of Meddies are observed; most notably in line IAM-3. By and large, lateral stratification is present in all sections, though less coherent in parts of IAM-9 and IAM-11, where the lamina seem more broken up and disperse, especially near the continental shelf. A visual comparison of line IAM-3 (farthest upstream) with IAM-11 (farthest downstream) shows generally degraded lateral stratification. This agrees with previous works that the undercurrent entrains and mixes with NACW, while becoming more diluted and losing kinetic energy, (eg. Johnson et al., [1994], Iorga and Lozier [1999a]).

This study of the Mediterranean Undercurrent by analysis of seismic data corroborates historical oceanographic data in this area. Seismic data show some decreasing lateral coherency from line IAM-3 to line IAM-11. This is in good agreement with salinity decreases from the historical oceanographic data. All temperature cross-sections from IAM-3 to IAM-11 show a relatively stable temperature profile. Temperature for the Mediterranean Undercurrent ranges from about 10 to 14 degrees for all lines. Salinity values however, decrease markedly from south to north. Line IAM-3 has MW salinity values from 36 psu, exceeding 36.5 psu. Line IAM-5 MW salinity varies between 36 psu and approximately 36.3 psu. Line IAM-9 displays much more constrained values, generally between 36 psu and 36.2 psu, with the exception of a higher salinity lens in the western portion of the line. Finally, line IAM-11 shows a sharp drop in salinity, with values near 36 psu. It also shows a high salinity lens in the western part of the line.

Homogeneity in the solid earth is represented seismically by transparency to wave propagation. Seismic boundaries are imaged. Likewise, well-mixed, or fully homogeneous zones in the open ocean fully transmit seismic energy and thus, do not produce reflections. No medium is perfectly homogeneous however, there is always some level of wave disturbance (reflection, refraction,

diffraction, etc). In zones approaching homogeneity, we expect less lateral seismic coherency further downstream in the Mediterranean Undercurrent. While this result is not on its own, conclusive, and more analysis is ongoing, there is come agreement between decreasing salinity and decreasing seismic coherency. Efforts are being made to quantify this relationship.

These result suggest that with increased mixing and dilution along the path of the undercurrent, we observe a stable temperature gradient, but decreasing salinity. Given the relatively uniform temperature, decreasing salinity may play a larger role in explaining the trend toward decreasing lateral coherency observed in the seismic data.

This Mediterranean Undercurrent study via analysis of IAM lines is informative. It corroborates historical oceanographic data from the area. However, an important caveat is that the study lacks *simultaneous* oceanographic and seismic acquisition to directly correlate reflection coefficient to in-situ physical property boundaries within the ocean. We can correlate the general structure of the Mediterranean Undercurrent but we cannot discuss in detail how internal thermohaline finestructure may vary over time, and therefore, if what we observe are persistent or reoccurring structures.

Studies, such as those of Ochoa and Bray, [1991], Johnson et al., [1994] and Iorga and Lozier [1999a], show that salinity dilution is occurring along the path of the undercurrent. Based on this observed dilution pattern, our data qualitatively corroborate historical data. Nevertheless, quantitative analysis as well as a simultaneous and co-located seismic and oceanographic survey designed over the path of the undercurrent would be a good way to firmly establish if there is a strong correlation and if this correlation persists over time.

5 - THE "GO" EXPERIMENT

The GO (Geophysical Oceanography) experiment was conceived to address questions about ocean processes that seismic imaging or physical oceanography alone cannot. For instance, what is the quantitative relationship between reflection coefficient and physical property contrasts in the ocean? What constraints can be set by combining seismic with simultaneous and co-located oceanographic measurements? Over what time scale do fine scale acoustic impedance contrasts change? What are the logistical and technical hurdles to overcome to found seismic oceanography as a unique scientific discipline?

Since seismic reflectivity is proportional to the contrast in density and sound speed of the media (eq. 8), to emphasize the usefulness of the seismic reflection profiling in oceanography, we chose the Gulf of Cadiz as our zone of interest because of the strong contrast in temperature and salinity between the Mediterranean Water and the surrounding Atlantic Waters, among other reasons (see Section 3.1). Indeed, Mediterranean Water is characterized by a relatively high temperature and salinity. Moreover, the Gulf of Cadiz has been extensively studied both oceanographically (eg. Madelain, [1970], Ochoa and Bray, [1991], Johnson et al., [1994], Bower, [1997], Richardson, [2002], Serra and Ambar [2002], among others) as well as seismically (eg. Biescas et al., 2008), thus providing a large historical database from which to constrain our interpretation.

The GO project was the first joint seismic and oceanographic survey in the Gulf of Cadiz. Before seismic reflection acquisition, we deployed moored Ocean Bottom Hydrophones (OBH) to measure wide angle refracted waves from the source. We set into place moored and ocean bottom current profilers, useful for making Eulerian measurements such as current velocity. While acquiring the seismic data we deployed oceanographic equipment such as expendable temperature/conductivity (salinity) probes at regular intervals in order to correlate reflection coefficient to temperature/salinity interfaces. From these and standard CTD casts we were able to calculate variations in sound speed. We found remarkable agreement between sound speed and reflection coefficient (eq. 8), indicating that sound speed is the dominant factor influencing reflection coefficient, Sallàres, [2008], (figure 16).

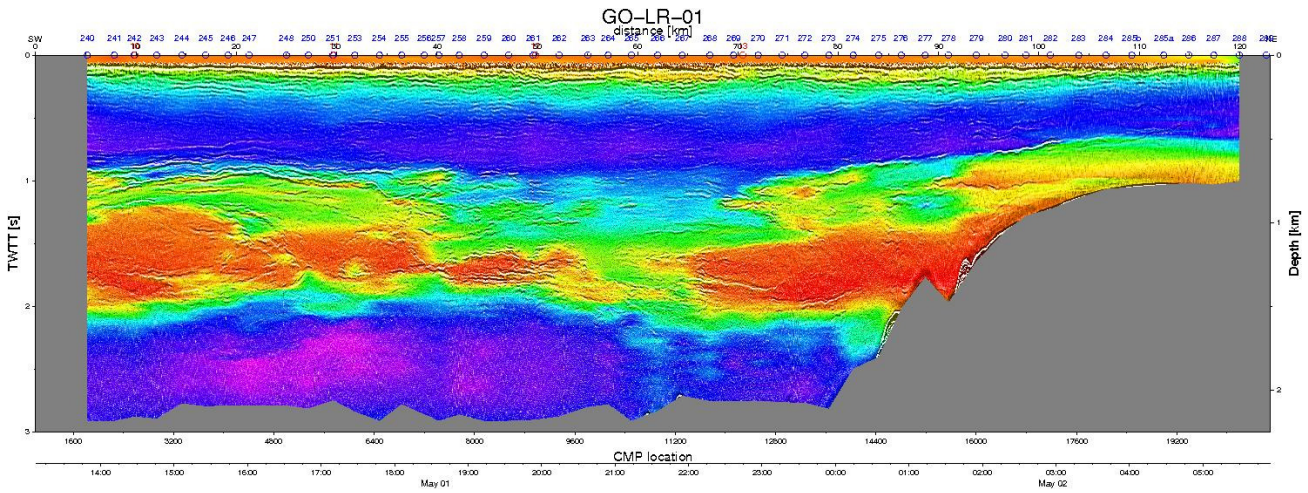

Figure 16 – Colour map of sound speed overlaid on co-located and simultaneously acquired seismic data. Warmer colours (red) correspond to higher sound speed, colder colours (blues, purples) correspond to lower sound speeds. There is a remarkable correlation between sound speed and seismic reflectivity. But, how to salinity and temperature each influence sound speed? How does density affect sound speed?

In addition, we recorded over the same geographical location several times to measure the temporal variability of thermohaline finestructure. We found that in as little as three hours (the time necessary to reverse ship heading and re-record) subtle changes in structures were obvious, whereas the larger overall structure persisted (figure 17).

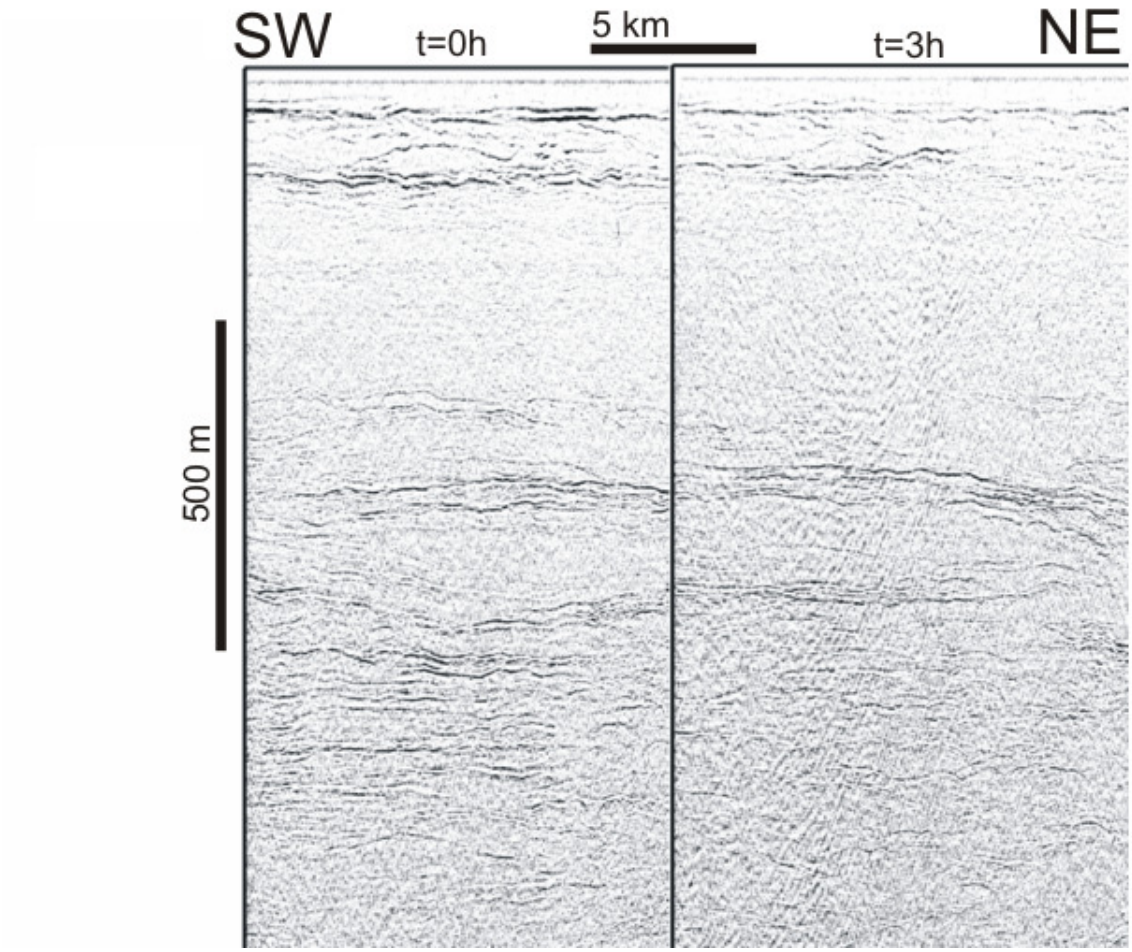

Figure 17 – Two brute stack images from the GO survey in April-May, 2007. The right panel shows thermohaline finestructure recorded 3 hours later. Note the presence of the overall structure, but subtle variations, Geli and Cosquer, [2008].

Seismic acquisition during the GO project was undertaken in two legs, testing a range of seismic source and receiver patterns. These included a small volume source array of 117 cu. in. (1.9 L) giving frequencies up to 200 Hz, a conventional seismic source of 5-50 Hz and a "flip-flop" source that combined low and high frequency (ie. resolution) sources (5-50 Hz and 10-100Hz). The combination of low and high frequency data sets provided a complementary view of ocean fine structure. The low resolution gave a better overall image, while the high showed finer details not resolved by the lower frequencies, but with less depth/distance of penetration. To this end, it is advantageous to apply a range of sources to cover a wider frequency bandwidth and thus better represent ocean fine structure.

Recent analysis provides stunning pictures of oceanic thermohaline fine structure. However, it is limited in its informative value without advanced analyses such as careful study of amplitude variation as a function of temperature and salinity. The ultimate goal is to understand the temperature and salinity partial contributions to acoustic impedance. Moreover, analysis of archived seismic data

without simultaneously acquired oceanographic data limits the interpretive potential. In the near future, I will be testing full-waveform tomography and inversion of seismic data to determine the 2D velocity structure of the ocean using a priori oceanographic acquired velocities as well as studying in more detail the quantitative relationship between temperature/salinity and acoustic impedance (density and sound speed). That is, the partial contribution of temperature and salinity to acoustic impedance in various regimes.

6 - THE OCEAN-CLIMATE INTERACTION AND GLOBAL CLIMATE CHANGE

Increasingly, climate studies are of more interest as we understand the importance of a healthy biosphere and a functioning, sustainable human civilization, in harmony with all life on Earth. We see that certain trends (warming) are predictable in a broad sense and that human influence is, at the very least, not negligible. However, interactions within the biosphere are complex and display emerging, non-linear properties that are not completely predictable nor fully understood.

The specific heat of sea water is much higher than that of air, having an enormous influence on the concentrations of heat energy on the Earth. In this respect, the upper 3 m of the ocean contain as much heat as the entire atmosphere, and therefore, the ocean is able to transport tremendous amounts of heat. Given the ocean's large heat budget, changes in surface temperature by only a degree or two can affect weather globally, [Ingmanson and Wallace, 1995]. Moreover, there have been observed changes in ocean circulation from those lasting a few years, such as El Niño, [Trenberth, 2001], to decadal changes such as those seen in Meddy circulation, [Richardson et al., 2000], or the so called 'great salinity anomalies' in the North Atlantic detailed by [Dickson et al., 1988] and [Belkin et al., 1998]. Analysis of archived 'Legacy' seismic data from these areas offers a new view of changing ocean patterns through identification of variations in temperature and salinity over seasonal, annual or decadal periods.

In only recent years we have learned that the earth's climate has changed dramatically on a scale of as little as a human lifetime. This discovery is in stark contrast to the traditional view that the climate change is so slow, as to be imperceptible. Paleoclimatic studies and computer modeling have demonstrated that global climate change can indeed occur rapidly (eg. Gates, [1976]; Barron, [1983]; Maier-Reimer et al., [1990]; Broecker, [2000]; Broecker, [2001]; Maslin et al., [2001]; Hoffman and Schrag, [2002]; International Panel on Climate Change Report, [2007]). However, ocean current computer modeling has limitations based on available historical data, when tested beyond their known validity. Above all, we cannot hope to predict with great accuracy, future ocean circulation and mixing trends, without fundamentally understanding the physics involved in these processes. Analysis of past seismic data has a unique opportunity to contribute to this ocean knowledge base by offering a measurement of circulation and mixing variability on the time scale of the available historical data, and by comparison with in-situ measurements.

Recently, considerable attention has been paid to probable *anthropogenic* climate change. Increased emission of green house gases such as carbon dioxide or methane are 'very likely' modifying

the composition of the atmosphere, [International Panel on Climate Change Report, 2007]. The increased carbon dioxide in the atmosphere is promoting a global warming trend. Furthermore, increased levels of carbon dioxide in the atmosphere, in turn modify the composition of the ocean through acidification. The byproduct of acidification of the oceans is higher levels of carbonic acid, which therefore affects biological processes, with unknown consequences. Ocean acidification levels are already observed to be 30% higher than those at the start of the industrial revolution, [Spratt and Sutton, 2008], influencing life in the oceans, and therefore, the entire food chain.

A deep understanding of all ocean processes (biological, chemical and physical), and their influence on one another is necessary to make reliable predictions about future trends, whether through computer modeling or otherwise. Analysis of data already available in archived seismic data sets, acquired over the past several decades can improve our understanding of physical ocean processes. To this end, it may even be possible to somewhat modify and influence our behavior as influential inhabitants of this planet.

7 - CONCLUSIONS

Analysis of seismic data from along the path of the Mediterranean Undercurrent show the robustness of the seismic reflection method to imaging thermohaline fine structure on a medium to large scale. Stacked sections show clear reflectivity and define three distinct water masses, that I identify as North Atlantic Central Water, Mediterranean Water and North Atlantic Deep Water. Interpretation of seismic lines show various physical oceanographic features, such as laminar stratification, areas of possible turbulence and Mediterranean Water eddies (Meddies). Due to the fact that reflection coefficient varies according to sound speed and density, at any given pressure, temperature and salinity may affect sound speed and density to varying degrees depending on the region of the ocean and the mixing processes involved. More analysis must be done to determine the partial contributions of temperature and salinity to both density and sound speed in a given regime.

It is known from oceanographic studies that the Mediterranean Undercurrent dilutes as it moves northward along the coast of Iberia. In this way I expected to see degrading lateral stratification in the seismic data as the water masses become more well-mixed and homogeneous, resulting in decreasing acoustic impedance contrasts from south to north. However, this relationship is not conclusive but does warrant further analysis.

Understanding the oceans is paramount to understanding the biosphere. The ocean covers some 70% of the planet's surface and it has a large heat budget. It is therefore very influential to the biosphere. Seismic Oceanography, particularly in joint interpretation with well-established oceanographic techniques provides the framework to visualize the ocean in a different manner, not directly in-situ with sparse measurements of salinity, temperature and pressure, but indirectly in dense grid spacings, by observing reflectivity of acoustic impedance boundaries.

Seismic reflection profiling is a well developed method that has been employed successfully for decades to image acoustic impedance contrasts in the solid earth. The principal advantage of the method over other oceanographic remote sensing techniques is its unprecedented horizontal resolution (approximately 2 orders of magnitude greater). In this way it is highly complementary to the very high vertical resolution already available with oceanographic methods to model the ocean. Seismic reflectivity within the ocean have been know to exist from some time, but until recently was not given much interest. Contemporary awareness of climate change and the Ocean's role in it has changed that.

Because of the high heat capacity of water, large scale circulation within the ocean is important for the global redistribution of heat and thereby, as a climate moderator. For instance, it is well known that warm water is transported north by the Gulf Stream, which in turn influences somewhat, the climate of Europe, making it warmer than a similar latitude intra-continental climate.

Interest in climate change, whether natural or anthropogenic, presents an opportunity to use seismic data to visualize the ocean in a different way. Thus, it may be possible to improve our knowledge of ocean circulation and perhaps deduce possible future climate trends.

ACKNOWLEDGEMENTS

I acknowledge the financial contributions of the GO project, part of the EU-NEST (European Union – New and Emerging Science and Technology) scholarship to complete this work as well as financial contributions from GEOCEAN. I would like to personally thank my director Ramón Carbonell and other European colleagues of the GO project, especially Berta Biescas, Valentí Sallàres, Francis Machín and Jose Lluis Pelegrí in Barcelona as well as Richard Hobbs in the UK and Dirk Klaschen in Germany for so much advice and support. Finally, to my wife Anna, for everything else.

REFERENCES

Ambar I., L. Armi, A. Bower, T. Ferreira (1999), Some aspects of time variability of the Mediterranean Water off south Portugal, *Deep-Sea Research*, **46** (1999) 1109-1136.

Armi, L. D., D. Hebert, N. Oakey, J.F. Price, P.L. Richardson, H.T. Rossby, and B. Ruddick (1989), Two years in the life of a Mediterranean salt lens, *J. Phys. Oceanog.*, **19**, 354–370.

Baringer, M. and J.F. Price (1997), Mixing and spreading of the Mediterranean outflow, *J. Phys. Oceanog.*, **V27**, pp. 1654-1677.

Barron, E.J. (1983), A warm equable Cretaceous: the nature of the problem, *Earth-Science Reviews*, **19**, 305-338.

Batchelor, G.K. (1957), Symposium on naval hydrodynamics, pp. 409-423, *National Academy of Sciences*, Washington, D.C..

Belkin, I.M., S. Levitus, J. Antonov and S.-A. Malmberg (1998), Great salinity anomalies in the North Atlantic., *Prog. Oceanogr.*, **41**, 1-68.

Biescas, B., V. Sallàres, J.L. Pelegrí, F. Machin, R. Carbonell, G. Buffett, J.J. Dañobeita, A. Calahorrano (2008), Imaging meddy finestructure using multichannel seismic reflection data, *Geophys. Res. Lett.*, doi:10.1029/2008GL033971, in press., accepted 2 May 2008.

Bower, A.S., L. Armi, I. Ambar (1997), Lagrangian Observations of Meddy Formation during A Mediterranean Undercurrent Seeding Experiment, *J. Phys. Oceanog.* **27**, pp. 2545-2575.

Bower, A.S., N. Serra, I. Ambar (2002), Structure of the Mediterranean Undercurrent and Mediterranean Water spreading around the southwestern Iberian Peninsula, *J. Geophys. Res.*, **107(C10)**, 3161, doi:10.1029/2001JC001007, 2002.

Brandt, A. (1975), Acoustic returns from density fluctuations in turbulent jets, *Oceans*, **75**, IEEE, New York.

Broecker, W.S. (2000), Was a change in thermohaline circulation responsible for the Little Ice Age?, *Proc. Nat. Acad. Sci.*, **97(4)**: 1339-1342.

Broecker, W.S. (2001), The big climate Amplifier Ocean Circulation-Sea Ice-Storminess-Dustiness-Albedo, *The Oceans and Rapid Climate Change: Past, Present, and Future, Geophysical Monograph 126*, American Geophysical Union, pp. 53-56.

Chan, W. and T. Motoi (2003), Effects of stopping the Mediterranean outflow on the southern polar region, *Polar Meteorol. Glaciol.*, **17**, 25-35.

Chernov, L.A. (1957), Correlation of amplitude and phase fluctuations of a wave propagating in a medium with random inhomogeneities (in Russian), *Akust. Zh.*, **3**, 192.

Chérubin, L.M., N. Serra and I. Ambar (2003), Low frequency variability of the Mediterranean Undercurrent downstream of Portimão Canyon, *J. Geoph. Res.*, **108**, 3, 3058, doi:

10.1029/2001JC001229

Claerbout, J. F. (1976), Fundamentals of geophysical data processing (with applications to petroleum prospecting), *McGraw-Hill, Inc.*, ISBN: 0-07-011117-0

Climate Change 2007 - The Physical Science Basis
Contribution of Working Group I to the Fourth Assessment Report of the IPCC
(ISBN 978 0521 88009-1 Hardback; 978 0521 70596-7 Paperback).

Cox, M.J.G. (1999), Static corrections for seismic reflection surveys, *Society of Exploration Geophysicists*, ISBN: 1-56080-080-1, pp. 352-364.

Daniault, N., J.P. Mazé, and M. Arhan (1994), Circulation and mixing of Mediterranean water west of the iberian peninsula, *Deep Sea Res.*, Part I, **41**, 1614-1685.

Dickson, R.R., J. Meineke, S.-A. Malmberg, A.J. Lee (1988), The 'great salinity anomaly' in the northern North Atlantic. *Prog. Oceanogr.*, **20**, 103-151.

Finch, D. (1985), Traces through time, a history of geophysical exploration for petroleum in Canada, *Canadian Society of Exploration Geophysicists*, ISBN: 0-9692354-0-2, p. 13.

Gates, W.L. (1976), The numerical simulation of ice-age climate with a global general circulation model, *J. Atmosp. Sci.*, **33**, 1844-1873.

Geli, L. and Cosquer, E. (2008), in preparation.

Gonella, J. and D. Michon (1988), *C.R. Acad. Sci. Paris Ser. II* **306**, 781.

Goodman, L. (1990), Acoustic scattering from ocean microstructure, *J. Geophys. Res.*, **95(C7)**, pp. 11,557-11,573.

Hatton, L., M.H. Worthington and J. Makin, Seismic Data Processing, Theory and Practice, *Blackwell Scientific Publications*, ISBN: 0-632-01374-5.

Haury, L.R., P.H. Wiebe, M.H. Orr, and M.G. Briscoe (1983), Tidally generated high-frequency internal wave packets and their effects on plankton in Massachusetts Bay, *J. Mar. Res.*, **41**, 65-112.

Heezen, B. C., and G. L. Johnson, 1969: Mediterranean Undercurrent and microphysiography west of Gibraltar. *Bull. Inst. Oceanogr.* Monaco, **67** (1382), p. 95.

Hoffman, P.F. and D.P. Schrag (2002), The Snowball Earth hypothesis: testing the limits of global change, *Terra Nova*, **14**, 129-155.

Holbrook, W.S., and I. Fer (2005), Ocean internal wave spectra inferred from seismic reflection transects, *Geophys. Res. Lett.*, **32**, L15604, doi: 10.1029/2005GL023733.

Holbrook, W.S., P. Páramo, S. Pearse, R.W. Schmitt (2003), Thermohaline fine structure in an oceanographic front from seismic reflection profiling, *Science*, **301**, pp.821-824.
Ingmanson, D.E. and Wallace, W.J. (1995), Oceanography - fifth edition, *Wadsworth Publishing Company,* ISN 0-534-24258-8

Iorga, M.C. and M.S. Lozier (1999a), Signatures of the Mediterranean outflow from a North Atlantic climatology, 1, Salinity and density fields, *J. Geophys. Res.*, **104(C11)**, 25,985-26,029.

Johnson, G.C., T.B. Sanford and M. O'Neil Baringer (1994), Stress on the Mediterranean Outflow Plume: Part I. Velocity and Water Property Measurements, *J. Phys. Oceanogr.*, **24**, 2072-2083.

Jones, I. F., and Levy, S., 1987, Signal-to-noise ratio enhancement in multichannel seismic data via the Karhunen-Loeve transform, *Geophysical Prospecting*, **35**,12-32.

Knauss, John A. (1997), Introduction to Physical Oceanography – second edition, *Prentice-Hall Inc., Simon & Schuster*, ISBN 0-13-238155-9.

Lockheed Martin Corp. (2005), Expendable Profiling Systems, Lockheed Martin Maritime Systems & Sensors, An ISO9001:2000 Company, SEPT2005/NDCR/20050054/Covers:2005.

Madelain, F. (1970), Influence de la topographie du fond sur l'ecoulement Mediterranee entre le Detroit de Gibraltar et le Cap Saint-Vincent. *Cahiers Oceanographiques*, **22(1)**, 43–61.

Maier-Reimer, E., U. Mikolajewicz and T. Crowley (1990), Ocean general circulation model sensitivity experiment with an open central American isthmus, *Paleooceanography*, **5**, 349-366.

Maslin, M., D. Seidov, J. Lowe, (2001), Synthesis of the nature and causes of rapid climate transitions during the quaternary, *The Oceans and Rapid Climate Change: Past, Present, and Future, Geophysical Monograph 126*, American Geophysical Union, pp. 9-52.

Munk, W.H. and J.C.R. Garrett (1973), Internal wave breaking and microstructure (The chicken and the egg), *Boundary Layer Meteorol.*, **4**, 37-45.

Munk, W.H. and C. Wunsch (1979), Ocean acoustic tomography: a scheme for large scale monitoring, *Deep-Sea Res.*, **26A**, 123-161.

Munk, W.H. and C. Wunsch (1998), Abyssal recipes II: energetics of tidal and wind mixing, *Deep-Sea Res. I*, **45**, 1977-2010.

Nandi, P., W.S. Holbrook, P. Páramo, S. Pearse, R.W. Schmitt (2004), Seismic reflection imaging of water mass boundaries in the Norwegian Sea, *Geophys. Res. Lett.*, **31**, L23311, doi:10.1029/2004GL021325.

Nakamura, Y., T. Noguchi, T. Tsuji, S. Itoh, H. Niino and T. Matsuoka (2006), Simultaneous seismic reflection and physical oceanographic oberservations of oceanic fine structure in the Kuroshio extension front, *Geophys. Res. Lett.*, **33**, L23605, doi:10.1029/2006GL027437.

Ochoa, J., and N.A. Bray (1991), Water mass exchange in the Gulf of Cadiz, *Deep-Sea Res.*, **38** (Suppl. 1), S465-S503.

Orr, M.H., and F.R. Hess (1978), Remote acoustic monitoring of natural suspensate distributions, active suspensate and slope/shelf water intrusions, *J. Geophys. Res.*, **83**, 4062-4068.
Ottersten, H. (1969), Atmospheric structure and radar backscattering in clear air, *Radio Sci.*, **4**, 1179-1193.

Páramo, P., and W.S. Holbrook (2005), Temperature contrasts in the water column inferred from

amplitude-versus-offset analysis of acoustic reflections, *Geophys. Res. Lett.*, **32**, L24611, doi:10.1029/2005GL024533.

Phillips, J.D., and D.F. Dean (1991), Multichannel acoustic reflection profiling of ocean water mass temperature/salinity interfaces, *Ocean Variability and Acoustic Propagation*, edited by J. Potter and A. Warn-Varnas, pp. 199-214, Springer, New York.

Reid, J.L. (1979), On the contribution of the Mediterranean sea outflow to the Norwegian-Greenland Sea, *Deep-Sea Res.*, **26**, 1199-1223.

Richardson, P. L., D. Walsh, L. Armi, M. Schroder, and J.F. Price (1989), Tracking three Meddies with SOFAR floats, *J. Phys. Oceanog.*, **19**, 371–383.

Richardson, P.L., A.S., Bower, W. Zenk (2000), A census of Meddies tracked by floats, *Progress in Oceanography*, **45** (2000) 209-250.

Ross, T., R. Lueck (2003), Sound scattering from oceanic turbulence, *Geophys. Res. Lett.*, **30(6)**, 1344, doi:10.1029/2002GL016733, 2003.

Ruddick, B. (1992), Intrusive mixing in a Mediterranean salt lens – intrusion slopes and dynamical mechanisms, *J. Phys. Oceanog.*, **22**, pp. 1274-1285.

Ruddick, B. (2003), Sounding Out Ocean Fine Structure, *Science*, **301**, pp.772-773.

Rudnick, D. and R. Ferrari (1999), Compensation of horizontal temperature and salinity gradients in the ocean mixed layer, *Science*, **283**, 526-529.

Sallàres, V. (2008), in preparation.

Serra, N., and I. Ambar (2002), Eddy generation in the Mediterranean Undercurrent, *Deep-Sea Research II*, **49**, 4225-4243.

Serra, N. (2007), Personal communication.

Sheriff, R.E. (1991), Encyclopedic Dictionary of Exploration Geophysics, 3rd ed., *Society of Exploration Geophysics*, ISBN 1-56080-018-6.

Sheriff, R.E. and Geldart, L.P., Exploration Seismology, History, Theory and Data Acquisition, Vol. 1, *Cambridge University Press*, ISBN 0-521-24373-4.

Spratt, D. and P. Sutton (2008), Climate 'code red' The case for a sustainable emergency, *Friends of the Earth* in conjunction with *Carbon Equity* and *Greenleap Strategic Institute*, ISBN: ISBN 978-1-920767-08-2

Stanton, T. K., D. Chu and P.H. Wiebe (1996), Acoustic scattering characteristics of several zooplankton groups, – *ICES Journal of Marine Science*, **53**, 289–295.

Stephens, J.C., and D.P. Marshall (1999), Dynamics of the Mediterranean salinity tongue, *J. Phys. Oceanog.*, **29**, 1425-1441.

Stern, M. E., (1960), The ''salt fountain'' and thermohaline convection. *Tellus,* **12,** 172–175.

Taner, M.T. and F. Koehler. (1969), Velocity Spectra – digital computer derivation and applications of velocity functions, *Geophysics*, **39**, 859-881.

Tatarski, V.I. (1971), The effects of turbulent atmosphere on wave propagation, *U.S: Dep. Commer. Publ.* **TT-68-50464**, pp.153-162, Israel Program for Scientific Translation, Jerusalem.

Thorpe, S.A. (2005), The Turbulent Ocean, *Cambridge Univ. Press*, New York, ISBN-13 978-0-521-83543-5.

Trenberth, K.E. (2001), El Niño Southern Oscillation (ENSO), Encyclopedia of Ocean Sciences, ed. J.H. Steele, S.A. Thorpe, and K.K. Turikian, vol, **5**; *London: Academic Press*, pp. 2599-2604.

Udías Vallina, Agustín, Principles of Seismology, (1999) *Cambridge University Press*, ISBN 0 521 62478 9

Warner, M. (1990), Absolute reflection coefficients from deep seismic reflections, *Tectonophysics*, **173**, 15-23.

Widess, M. (1973), How thin is a thin bed?, *Geophysics*, **38**, 1176-1180.

Xu, X, E.P. Chassignet, J.F. Price, T.M. Özgökmen, H. Peters. (2007), A regional modeling study of the entraining Mediterranean outflow, *J. Geophys. Res.*, **112**, C12005, doi:10.1029/2007JC004145, 2007.

Yilmaz, O. (1987), Seismic Data Processing, *Soc. of Explor. Geophys.*, ISBN 0-931830-41-9 (Series 1), ISBN 0-931830-40-0 (Volume 2).

APPENDIX 1

Processing flows for Iberian-Atlantic Margin lines

(note: text in bold was not applied for true amplitude analysis, only for display)

IAM-3

FLOW - SEGY-IN Fri Jan 26 13:13:19 2007
  Output - SWG_old_but_good Add 490446 Over 0
(SHOTS WITH GEOMETRY APPLIED)
 SEG-Y Input

FLOW - total_flow Mon Jan 21 23:25:14 2008
  Output - evshots_v4 Add 490446 Over 0
 Linear Moveout Correction
  Type of LMO application Forward
  Header entry used to specify distance Absolute value of offset
  Get velocity file from the DATABASE? No
  SELECT Primary header entry Field file ID number
  SELECT Secondary header entry Absolute value of offset
  SPECIFY velocity parameters
   101:3000:1505
 Eigenvector Filter
  Mode Subtract Eigenimage of Zone
  Get matrix design gates from DATABASE? No
   SELECT Primary header word Field file ID number
   SPECIFY design time gate parameters
   101:0-500/
  Get application gates from DATABASE? No
   SELECT Primary header word Field file ID number
   SPECIFY application gate parameters
   101:0-500/
  Get Subtraction gates from DATABASE? No
   SELECT Primary header word Field file ID number
   SPECIFY subtraction gate parameters
   101:0-500/
  Type of Computations ? Real
  Horizontal window width 192
  Start percent of eigenimage range 0.
  End percent of eigenimage range 10.
 Linear Moveout Correction
  Type of LMO application Remove
 Bandpass Filter
  TYPE of filter Single Filter
  Type of filter specification Ormsby bandpass
  PHASE of filter Minimum
   Percent additive noise factor 1.
  Apply a notch filter? No
  Ormsby filter frequency values 8-15-90-100

FLOW - total_flow Tue Jan 22 11:16:47 2008
  Output - ev_stack_vels4 Add 14903 Over 0
 True Amplitude Recovery
   Basis for spherical spreading 1/dist
   Should the velocity be treated as No
  space variable?
    Specify TAR velocity function
   0-1505/
   dB/sec correction constant 6.
  APPLY function to data or REMOVE effect Apply
  of amplitude corrections?
  Maximum application TIME 0.
  Normalization reference TIME 0.
 Ensemble Gain
  Gain computation algorithm Stack traces
  Average amplitude normalization level 1.

First window start time (specification method) **Use default (trace start time)**
Maximum window start increment (msec) **40.**
Last window end time (msec) **Use default (trace end time)**
Maximum first window length (msec) **400.**
Maximum last window length (msec) **400.**
Zero amplitudes treatment **Exclude**
Type of output **Gained traces**
Big Vector data storage preference **Memory**
Diagnostic printout flag **0**
Normal Moveout Correction
Direction for NMO application FORWARD
Stretch mute percentage 0.
Apply any remaining static during NMO? No
Disable check for previously applied NMO? No
Apply partial NMO? No
Long offset correction? NONE
Get velocities from the database? Yes
SELECT Velocity parameter file vels4
CDP/Ensemble Stack
Sort order of input ensembles CDP
METHOD for trace summing Mean
Root power scalar for stack normalization 0.5
Apply final datum statics after stack? No

FLOW - total_flow Tue Jan 22 11:19:10 2008
Output - fx_stack_vels4 Add 14903 Over 0
F-X Decon
TYPE of filter Wiener Levinson
Percentage of white noise 0.
Horizontal window length 10
Number of filter samples 5
Time window length 1000.
Time window overlap 100.
F-X filter start frequency 1.
F-X filter end frequency 90.

FLOW - total_flow Wed Jan 23 12:49:18 2008
Output - psmig_stack_vels4 Add 14903 Over 0
Phase Shift Migration

FLOW - total_flow Wed Jan 23 12:54:16 2008
Output - final_stack_vels4 Add 14903 Over 0
Automatic Gain Control
Application mode **APPLY**
Type of AGC scalar **RMS**
AGC operator length **6000.**
BASIS for scalar application **Leading**
Robust Scaling? **No**
Time/Depth Conversion
Conversion direction Time-to-DEPTH
Maximum frequency of interest (in Hz) 120.
Percent velocity scale factor 100.
Get velocities from DATABASE? Yes
SELECT Velocity Parameter File vels4

IAM-5

FLOW - SEGY-IN Fri Jan 26 13:16:06 2007
Output - SWG_old_but_good Add 819264 Over 0
(SHOTS WITH GEOMETRY APPLIED)
SEG-Y Input

FLOW - total_flow Tue Jan 22 02:54:20 2008
Output - evshots_v4 Add 819264 Over 0
Linear Moveout Correction
Type of LMO application Forward
Header entry used to specify distance Absolute value of offset
Get velocity file from the DATABASE? No
SELECT Primary header entry Field file ID number
SELECT Secondary header entry Absolute value of offset
SPECIFY velocity parameters
101:3000:1505
Eigenvector Filter
Mode Subtract Eigenimage of Zone
Get matrix design gates from DATABASE? No
SELECT Primary header word Field file ID number
SPECIFY design time gate parameters
101:0-500/
Get application gates from DATABASE? No
SELECT Primary header word Field file ID number
SPECIFY application gate parameters
101:0-500/
Get Subtraction gates from DATABASE? No
SELECT Primary header word Field file ID number
SPECIFY subtraction gate parameters
101:0-500/
Type of Computations ? Real
Horizontal window width 192
Start percent of eigenimage range 0.
End percent of eigenimage range 10.
Linear Moveout Correction
Type of LMO application Remove
Bandpass Filter
TYPE of filter Single Filter
Type of filter specification Ormsby bandpass
PHASE of filter Minimum
Percent additive noise factor 1.
Apply a notch filter? No
Ormsby filter frequency values 8-15-90-100

FLOW - total_flow Tue Jan 22 08:11:57 2008
Output - ev_shots_limoff Add 742458 Over 0

FLOW - total_flow Wed Jan 23 14:13:47 2008
Output - evstack_v4 Add 14388 Over 0
True Amplitude Recovery
Basis for spherical spreading 1/dist
Should the velocity be treated as space variable? No
Specify TAR velocity function
0-1505/
dB/sec correction constant 6.
APPLY function to data or REMOVE effect of amplitude corrections? Apply
Maximum application TIME 0.
Normalization reference TIME 0.
Ensemble Gain
Gain computation algorithm Stack traces
Average amplitude normalization level 1.
First window start time (specification method) Use default (trace start time)
Maximum window start increment (msec) 40.
Last window end time (msec) Use default (trace end time)

Maximum first window length (msec) 400.
Maximum last window length (msec) 400.
Zero amplitudes treatment Exclude
Type of output Gained traces
Big Vector data storage preference Memory
Diagnostic printout flag 0
Normal Moveout Correction
Direction for NMO application FORWARD
Stretch mute percentage 0.
Apply any remaining static during NMO? No
Disable check for previously applied NMO? No
Apply partial NMO? No
Long offset correction? NONE
Get velocities from the database? Yes
SELECT Velocity parameter file vels4
CDP/Ensemble Stack
Sort order of input ensembles CDP
METHOD for trace summing Mean
Root power scalar for stack normalization 0.5
Apply final datum statics after stack? No

FLOW - total_flow Wed Jan 23 14:15:58 2008
Output - fxstack_v4 Add 14388 Over 0
F-X Decon
TYPE of filter Wiener Levinson
Percentage of white noise 0.
Horizontal window length 10
Number of filter samples 5
Time window length 1000.
Time window overlap 100.
F-X filter start frequency 1.
F-X filter end frequency 90.

FLOW - total_flow Wed Jan 23 14:35:23 2008
Output - migstack_v4 Add 14388 Over 0
Phase Shift Migration

FLOW - total_flow Wed Jan 23 14:39:11 2008
Output - final_stack_v4 Add 14388 Over 0
Automatic Gain Control
Application mode APPLY
Type of AGC scalar RMS
AGC operator length 6000.
BASIS for scalar application Leading
Robust Scaling? No
Time/Depth Conversion
Conversion direction Time-to-DEPTH
Maximum frequency of interest (in Hz) 120.
Percent velocity scale factor 100.
Get velocities from DATABASE? Yes
SELECT Velocity Parameter File vels4

IAM-9

FLOW - GEOM Wed Feb 14 11:34:53 2007
Output - SWG_8sec Add 884352 Over 0
Inline Geom Header Load
Compute and apply statics to sea level? No
Primary header to match database FFID
Secondary header to match database None
Match by valid trace number? No
Drop traces with NULL CDP headers? No
Drop traces with NULL receiver headers? No

FLOW - total_flow Tue Jan 22 03:35:21 2008
Output - evshots_v4 Add 884352 Over 0
Linear Moveout Correction
Type of LMO application Forward
Header entry used to specify distance Absolute value of offset
Get velocity file from the DATABASE? No
SELECT Primary header entry Field file ID number
SELECT Secondary header entry Absolute value of offset
SPECIFY velocity parameters
101:3000:1505
Eigenvector Filter
Mode Subtract Eigenimage of Zone
Get matrix design gates from DATABASE? No
SELECT Primary header word Field file ID number
SPECIFY design time gate parameters
101:0-600/
Get application gates from DATABASE? No
SELECT Primary header word Field file ID number
SPECIFY application gate parameters
101:0-600/
Get Subtraction gates from DATABASE? No
SELECT Primary header word Field file ID number
SPECIFY subtraction gate parameters
101:0-600/
Type of Computations ? Real
Horizontal window width 192
Start percent of eigenimage range 0.
End percent of eigenimage range 10.
Linear Moveout Correction
Type of LMO application Remove
Bandpass Filter
TYPE of filter Single Filter
Type of filter specification Ormsby bandpass
PHASE of filter Minimum
Percent additive noise factor 1.
Apply a notch filter? No
Ormsby filter frequency values 8-15-90-100

FLOW - total_flow Tue Jan 22 08:29:20 2008
Output - evshots_limoff Add 801444 Over 0

FLOW - total_flow Tue Jan 22 12:27:52 2008
Output - evstack_v4 Add 26831 Over 0
True Amplitude Recovery
Basis for spherical spreading 1/dist
Should the velocity be treated as space variable? No
Specify TAR velocity function
0-1505/
dB/sec correction constant 6.
APPLY function to data or REMOVE effect of amplitude corrections? Apply
Maximum application TIME 0.
Normalization reference TIME 0.
Ensemble Gain
Gain computation algorithm Stack traces

Average amplitude normalization level 1.
First window start time (specification method) Use default (trace start time)
Maximum window start increment (msec) 40.
Last window end time (msec) Use default (trace end time)
Maximum first window length (msec) 400.
Maximum last window length (msec) 400.
Zero amplitudes treatment Exclude
Type of output Gained traces
Big Vector data storage preference Memory
Diagnostic printout flag 0
Normal Moveout Correction
Direction for NMO application FORWARD
Stretch mute percentage 0.
Apply any remaining static during NMO? No
Disable check for previously applied NMO? No
Apply partial NMO? No
Long offset correction? NONE
Get velocities from the database? Yes
SELECT Velocity parameter file vels4
CDP/Ensemble Stack
Sort order of input ensembles CDP
METHOD for trace summing Mean
Root power scalar for stack normalization 0.5
Apply final datum statics after stack? No

FLOW - total_flow Tue Jan 22 12:31:32 2008
Output - fxstack_v4 Add 26831 Over 0
F-X Decon
TYPE of filter Wiener Levinson
Percentage of white noise 0.
Horizontal window length 10
Number of filter samples 5
Time window length 1000.
Time window overlap 100.
F-X filter start frequency 1.
F-X filter end frequency 90.

FLOW - total_flow Wed Jan 23 13:13:04 2008
Output - migstack_v4 Add 26831 Over 0
Phase Shift Migration

FLOW - total_flow Wed Jan 23 13:18:05 2008
Output - final_stack_v4 Add 26831 Over 0
Automatic Gain Control
Application mode APPLY
Type of AGC scalar RMS
AGC operator length 6000.
BASIS for scalar application Leading
Robust Scaling? No
Time/Depth Conversion
Conversion direction Time-to-DEPTH
Maximum frequency of interest (in Hz) 120.
Percent velocity scale factor 100.
Get velocities from DATABASE? Yes
SELECT Velocity Parameter File vels4

IAM-11

FLOW - GEOM Tue Oct 30 14:07:33 2007
Output - SWG_8sec Add 554112 Over 0
Inline Geom Header Load
Compute and apply statics to sea level? No
Primary header to match database FFID
Secondary header to match database None
Match by valid trace number? No
Drop traces with NULL CDP headers? Yes
Drop traces with NULL receiver headers? Yes

FLOW - total_flow Mon Jan 21 23:55:41 2008
Output - evshots_v4 Add 554112 Over 0
Linear Moveout Correction
Type of LMO application Forward
Header entry used to specify distance Absolute value of offset
Get velocity file from the DATABASE? No
SELECT Primary header entry Field file ID number
SELECT Secondary header entry Absolute value of offset
SPECIFY velocity parameters
101:3000:1505
Eigenvector Filter
Mode Subtract Eigenimage of Zone
Get matrix design gates from DATABASE? No
SELECT Primary header word Field file ID number
SPECIFY design time gate parameters
101:0-600/
Get application gates from DATABASE? No
SELECT Primary header word Field file ID number
SPECIFY application gate parameters
101:0-600/
Get Subtraction gates from DATABASE? No
SELECT Primary header word Field file ID number
SPECIFY subtraction gate parameters
101:0-600/
Type of Computations ? Real
Horizontal window width 192
Start percent of eigenimage range 0.
End percent of eigenimage range 10.
Linear Moveout Correction
Type of LMO application Remove
Bandpass Filter
TYPE of filter Single Filter
Type of filter specification Ormsby bandpass
PHASE of filter Minimum
Percent additive noise factor 1.
Apply a notch filter? No
Ormsby filter frequency values 8-15-90-100

FLOW - total_flow Tue Jan 22 05:23:39 2008
Output - evshots_limoff Add 502164 Over 0

FLOW - total_flow Tue Jan 22 11:34:08 2008
Output - evstack_v4 Add 17484 Over 0
True Amplitude Recovery
Basis for spherical spreading 1/dist
Should the velocity be treated as space variable? No
Specify TAR velocity function
0-1505/
dB/sec correction constant 6.
APPLY function to data or REMOVE effect of amplitude corrections? Apply
Maximum application TIME 0.
Normalization reference TIME 0.
Ensemble Gain
Gain computation algorithm Stack traces

Average amplitude normalization level **1.**
First window start time (specification method) **Use default (trace start time)**
Maximum window start increment (msec) **40.**
Last window end time (msec) **Use default (trace end time)**
Maximum first window length (msec) **400.**
Maximum last window length (msec) **400.**
Zero amplitudes treatment **Exclude**
Type of output **Gained traces**
Big Vector data storage preference **Memory**
Diagnostic printout flag **0**
Normal Moveout Correction
Direction for NMO application FORWARD
Stretch mute percentage 0.
Apply any remaining static during NMO? No
Disable check for previously applied NMO? No
Apply partial NMO? No
Long offset correction? NONE
Get velocities from the database? Yes
SELECT Velocity parameter file vels4
CDP/Ensemble Stack
Sort order of input ensembles CDP
METHOD for trace summing Mean
Root power scalar for stack normalization 0.5
Apply final datum statics after stack? No

FLOW - total_flow Tue Jan 22 11:36:41 2008
Output - fxstack_v4 Add 17484 Over 0
F-X Decon
TYPE of filter Wiener Levinson
Percentage of white noise 0.
Horizontal window length 10
Number of filter samples 5
Time window length 1000.
Time window overlap 100.
F-X filter start frequency 1.
F-X filter end frequency 90.

FLOW - total_flow Wed Jan 23 13:18:25 2008
Output - migstack_v4 Add 17484 Over 0
Phase Shift Migration

FLOW - total_flow Wed Jan 23 13:21:35 2008
Output - final_stack_v4 Add 17484 Over 0
Automatic Gain Control
Application mode **APPLY**
Type of AGC scalar **RMS**
AGC operator length **6000.**
BASIS for scalar application **Leading**
Robust Scaling? No
Time/Depth Conversion
Conversion direction Time-to-DEPTH
Maximum frequency of interest (in Hz) 120.
Percent velocity scale factor 100.
Get velocities from DATABASE? Yes
SELECT Velocity Parameter File vels4

APPENDIX 2

High resolution annotated stacks for Iberian-Atlantic Margin lines

Corresponding files:

IAM3_annotated.pdf
IAM5_annotated.pdf
IAM9_annotated.pdf
IAM11_annotated.pdf